The Power of Transient Piezometric Head Data in Inverse Modeling: An Application of the Localized Normal-score EnKF with Covariance Inflation in a Heterogenous Bimodal Hydraulic Conductivity Field

Teng Xu[a,b,*], J. Jaime Gómez-Hernández[b], Haiyan Zhou[b], Liangping Li[b]

[a] *School of Water Resources and Environment, China University of Geosciences, 29 Xueyuan Lu, 100083, Beijing, China*

[b] *Research Institute of Water and Environmental Engineering, Universitat Politècnica de València, 46022, Valencia, Spain*

Abstract

The localized normal-score ensemble Kalman filter (NS-EnKF) coupled with covariance inflation is used to characterize the spatial variability of a channelized bimodal hydraulic conductivity field, for which the only existing prior information about conductivity is its univariate marginal distribution. We demonstrate that we can retrieve the main patterns of the reference field by assimilating a sufficient number of piezometric observations using the NS-EnKF. The possibility of characterizing the conductivity spatial variability using only piezometric head data shows the importance of accounting for these data in inverse modeling.

Keywords: Normal score transform, Localization, Covariance inflation, Ensemble Kalman filter, Filter divergence

1. Introduction

It is well known that proper characterization of subsurface hydrogeologic properties and their uncertainty are critical issues for groundwater forecast, subsurface resource management and environmental risk assessment [1]. This can be achieved by stochastic inverse modeling accounting for real-time state data. Some existing methods for stochastic inverse modeling are the gradual deformation method, the sequential self-calibration, the Markov chain Monte Carlo method, the Representer method, and the Pilot Points method [e.g., 2, 3, 4, 5, 6, 7, 8, 9, 10]. Although these methods are flexible with regard to nonlinearities and system complexity, they are very time consuming and not easy to apply to large scale problems [11].

*Corresponding author. Tel: +34 963879615 Fax: +34 963879492

Email addresses: tenxu@posgrado.upv.es (Teng Xu), jaime@dihma.upv.es (J. Jaime Gómez-Hernández), haizh@upvnet.upv.es (Haiyan Zhou), liali@upvnet.upv.es (Liangping Li)

To overcome this problem, the Ensemble Kalman Filter (EnKF) has become more popular in many fields, such as oceanography, meteorology, petroleum engineering, or hydrology [e.g., 12, 13, 14, 15, 16, 17, 11, 18], because it is computationally efficient and capable of handling large fields. However, it has been shown that, although the EnKF is good accounting for the non linearities of the state equation, it fails when dealing with non-Gaussian parameter fields [e.g., 19, 20, 21].

The particle filter (PF) [e.g., 22, 23, 24] is able to handle any type of statistical distribution and it is very robust for nonlinear models and non-Gaussian distributed variables [25]; however, it is also very time-consuming and hardly applied to large simulation models.

Recently, new methods have been developed trying to adapt the EnKF to non-Gaussian distributions. They can be grouped in four categories according to their characteristics: those using a Gaussian mixture model (GMM), those using a transformed reparameterization, the iterative EnKF, and those using a Gaussian anamorphosis (GA) also known as normal score (NS) transform.

In the first category, the methods using a Gaussian mixture model method apply a probabilistic model in which a finite number of Gaussian probability density functions (pdf's) is used to approximate the underlying non-Gaussian pdf's [e.g., 26, 19, 27, 28, 29, 30]. GMM takes advantage that for linear transfer functions the forecasting step preserves the Gaussian mixture. Sun et al. [19] showed the benefits of the EnKF integrated with GMM techniques for high-dimensional, multimodal parameter distributions. Dovera and Della Rossa [28] combined the EnKF with GMM for simulating a multimodal distribution in the context of reservoir facies modeling.

In the second category, the transformed reparameterization, the methods work with alternative state variables that may be better approximated by a Gaussian distribution. Chen and Oliver [31] discuss that using the EnKF to update saturation may yield non-physical results because of its non-Gaussian distribution. They proposed to reparameterize the formulation of the EnKF using the water arrival time as the state variable. This approach has also been followed by Chen et al. [21], Chang et al. [32], Li et al. [33].

In the third category, the iterative EnKF, an iterative scheme is introduced into the forecasting and updating steps of the EnKF. At any given time step, the static parameters are repeatedly updated using the Kalman gain equation until a satisfactory match between predicted state variables and observations is reached. This iteration is needed because of the strong non-linearities of the forecast model. Example applications can be found in the petroleum engineering literatures [e.g., 34, 35, 36, 37, 38, 39, 40, 41], and also in hydrogeology [11].

In the fourth category, the EnKF is combined with GA. Gaussian anamorphosis (also known as normal score transform) is used to transform the non-Gaussian variables into Gaussian ones, but only at the univariate level. Then the EnKF is used on the univariate Gaussian variables. Applications of this approach can be found in the fields of ecology, remote sensing, geophysics, petroleum engineering or hydrogeology [e.g., 20, 42, 17, 43, 44, 45, 25, 46, 47].

In this paper, we will apply the GA implementation by Zhou et al. [46] to a bimodal aquifer assuming that the only information we have about the hydraulic conductivity is its univariate distribution. Our conjecture is that the assimilation of enough transient piezometric head data is sufficient to capture the main features of the spatial variability of hydraulic conductivity.

The structure of this paper is as follows. First, an introduction of the GA implementation is given. And then we evaluate the impact of the number of conditioning piezometric heads in the characterization of the conductivity patterns. The paper ends with a summary of the main findings.

2. The Localized Normal-Score Ensemble Kalman Filter with Covariance Inflation

The Normal-Score Ensemble Kalman Filter (NS-EnKF) is an evolution of the EnKF to accommodate non-Gaussian random variables. It is based on a univariate transformation of each component of the parameter vector of non-Gaussian conductivities into another vector in which all components follow a standard Gaussian distribution.

We will present the NS-EnKF for the case in which we wish to characterize the heterogeneity of hydraulic conductivity (X) by assimilating transient piezometric heads (Y). The NS-EnKF can be summarized as follows:

1. Initialization step. An ensemble of hydraulic conductivity fields must be generated. There are many techniques that can be used for this purpose, such as sequential simulation, multiple point simulations with training images [e.g., 48, 49, 50]; however, since we assume that there is no prior information about the spatial heterogeneity, but only information about its marginal univariate distribution, we generate homogeneous realizations, each one with a value drawn from this distribution.
2. Normal-score transformation step. At each location, all conductivity values from all realizations are collected, and a normal score transform function is built. Then, these functions are used to transform all values for all realizations.

   The normal score transformed conductivity vector $\widetilde{\mathbf{X}}$ is

$$\widetilde{\mathbf{X}} = \phi(\mathbf{X}) \tag{1}$$

where $\phi(\cdot)$ is a vectorial normal score transform function, different for each location. Each member of the vectorial function is non-parametrically built.

3. Forecasting step. In this step, the simulated piezometric heads are calculated for the t^{th} time step based on the piezometric heads from the $(t-1)^{th}$ time step using a transient flow model, realization by realization.

$$\mathbf{Y}_t = \psi(\mathbf{Y}_{t-1}, \mathbf{X}_{t-1}) \tag{2}$$

where $\mathbf{Y}_t$, $\mathbf{Y}_{t-1}$ are the simulated piezometric heads at the t^{th} time step and the simulated piezometric heads at the $(t-1)^{th}$ time step, respectively; $\mathbf{X}_{t-1}$ is the conductivity estimate at the $(t-1)^{th}$ time step; $\psi(\cdot)$ denotes the transient groundwater flow model.

4. Analysis step or assimilation step. The aim of this step is to update the transformed conductivity $\widetilde{\mathbf{X}}$ and piezometric heads $\mathbf{Y}$ accounting for the discrepancy between forecasted and observed piezometric heads.

   (a) First, build the augmented state vector $\mathbf{S}$ with the transformed conductivity $\widetilde{\mathbf{X}}$ and the forecasted piezometric heads $\mathbf{Y}$, which for the i^{th} realization at the t^{th} time step is:

$$\mathbf{S}^f_{i,t} = \begin{bmatrix} \widetilde{\mathbf{X}} \\ \mathbf{Y} \end{bmatrix}_{i,t}, \tag{3}$$

   (b) Then, the measured piezometric heads at time t are assimilated by updating the state vector into $\mathbf{S}^a_{i,t}$ using:

$$\mathbf{S}^a_{i,t} = \mathbf{S}^f_{i,t} + \mathbf{G}_t(\mathbf{Y}^o_t + e_{i,t} - \mathbf{H}\mathbf{S}^f_{i,t}) \tag{4}$$

$$\mathbf{G}_t = \mathbf{P}_t\mathbf{H}^T(\mathbf{H}\mathbf{P}_t\mathbf{H}^T + \mathbf{R}_t)^T \tag{5}$$

   where $\mathbf{S}^a_{i,t}$ is the updated state vector of the i^{th} ensemble member at the t^{th} time step; $\mathbf{S}^f_{i,t}$ is the forecast state vector; $\mathbf{P}_t$ is the forecast covariance matrix; $\mathbf{Y}^o_t + e_{i,t}$ is the hydraulic head observation vector, including the true head $\mathbf{Y}^o_t$ plus the observation error $e_{i,t}$ —the observation error has with mean zero and covariance $\mathbf{R}_t$; $\mathbf{G}_t$ is the Kalman gain; and $\mathbf{H}$ is an observation matrix, which consists only of 0's and 1's when observations are taken at simulation nodes, in which case, Equation 5 can be simplified as

$$\mathbf{G}_t = \mathbf{C}_{\widetilde{X}Y}\big(\mathbf{C}_{YY} + \mathbf{R}_t\big)^{-1} \tag{6}$$

where $\mathbf{C}_{\widetilde{X}Y}$ corresponds to the cross-covariance between the transformed state vector and the forecasted piezometric heads at the observation locations; and $\mathbf{C}_{YY}$ is the covariance between the forecasted piezometric heads at the observation locations.

5. Back transformation step. Back transform the updated normal-score transformed conductivities into conductivities using the inverse of the previously computed transform functions:

$$\mathbf{X} = \phi^{-\mathbf{1}}(\widetilde{\mathbf{X}}) \tag{7}$$

since a non-parametric transformation is used, there is a need to specify how to backtransform the values that are outside the range given by the minimum and maximum values used to build the non-parametric transform function. In our case we used the same approach as described in the Gslib library [51] choosing a power interpolation with absolute bounds set at -4 and 4 ln(m/d).

6. Return to the step 3 and repeat the processes until all the observed data are assimilated.

Zhou et al. [46, 52] have shown that the NS-EnKF is a good alternative in the characterization of non-Gaussian distributed conductivity fields. However, since the NS-EnKF is based in the EnKF, it has the same drawbacks, that is, the appearance of spurious correlations between distant points and the underestimation of the final uncertainty. Spurious correlations appear due to the numerical nature of the covariance calculations, which result in fluctuating covariance estimates about zero at distances for which it should be zero. Underestimation of the final uncertainty is due to the underestimation of the empirical covariance based in a small number of realizations [53]. These two problems can be tackled through combining covariance localizations and covariance inflation techniques.

Covariance localization aims to eliminate the effect of spurious correlations among the state variables and the parameters by constraining the correlation range of the empirical covariance. This can be achieved by replacing Equation 6 with the following equation:

$$\mathbf{G}_t = \rho_{\widetilde{X}Y} \circ \mathbf{C}_{\widetilde{X}Y}\big(\rho_{YY} \circ \mathbf{C}_{YY} + \mathbf{R}_t\big)^{-1} \tag{8}$$

where $\circ$ represents the Schur product; and $\rho_{\widetilde{X}Y}$ and ρ_{YY} are localization functions used to correct $\mathbf{C}_{\widetilde{X}Y}$ and $\mathbf{C}_{YY}$, respectively.

There are many alternatives to calculate the localization functions [e.g., 54, 55, 56, 57, 58]. In this paper, we use the same fifth-order distance dependent localization function [e.g., 59, 60] for both covariances.

$$\rho_{\widetilde{X}Y}(d) = \rho_{YY}(d) = \begin{cases} -\frac{1}{4}(\frac{d}{a})^5 + \frac{1}{2}(\frac{d}{a})^4 + \frac{5}{8}(\frac{d}{a})^3 - \frac{5}{3}(\frac{d}{a})^2 + 1, & 0 \leq \text{d} \leq \text{a}; \\ \frac{1}{12}(\frac{d}{a})^5 - \frac{1}{2}(\frac{d}{a})^4 + \frac{5}{8}(\frac{d}{a})^3 + \frac{5}{3}(\frac{d}{a})^2 - 5(\frac{d}{a}) + 4 - \frac{2}{3}(\frac{d}{a})^{-1}, & \text{a} \leq \text{d} \leq \text{2a}; \\ 0 & \text{d>2a.} \end{cases} \tag{9}$$

where d is the Euclidean distance, and a is a distance parameter controlling the distance at which the localization function will die out to zero. We chose this function based on our past experience [18, 47].

Covariance inflation is a technique used to avoid filter divergence (inbreeding) by inflating the empirical covariance. This can be achieved by linearly inflating each component of the augmented state vector:

$$\mathbf{S}_{i,t}^{inf,f} = \sqrt{\lambda_t}(\mathbf{S}_{i,t}^f - \langle \mathbf{S}_t^f \rangle) + \langle \mathbf{S}_t^f \rangle \tag{10}$$

where $\mathbf{S}_{i,t}^{inf,f}$ is the i^{th} ensemble member at the t^{th} time step of the state vector; $\langle \cdot \rangle$ denotes ensemble average; λ_t is the inflation factor at the t^{th} time step. There are many methods to get the inflation factor λ [e.g., 61, 62, 63, 64, 65]. In this work, we will use the time-dependent inflation algorithm proposed by Wang and Bishop [66].

$$\lambda_t = \frac{(\mathbf{R}_t^{-\frac{1}{2}} d_t)^T \mathbf{R}_t^{-\frac{1}{2}} d_t - k_t}{trace\{\mathbf{R}_t^{-\frac{1}{2}} \mathbf{H} \mathbf{P}_t (\mathbf{R}_t^{-\frac{1}{2}} \mathbf{H})^T\}} \tag{11}$$

where k_t is the number of observations; d_t is the residual between observation data and forecast data, which can be described as:

$$d_t \equiv \mathbf{Y}_t^o + e_{i,t} - \mathbf{H}\langle \mathbf{S}_t^f \rangle \tag{12}$$

Then the transformed analysis state vector $\mathbf{S}_{i,t}^a$ is:

$$\mathbf{S}_{i,t}^a = \mathbf{S}_{i,t}^{inf,f} + \lambda_t \mathbf{C}_{\widetilde{X}Y}(\lambda_t \mathbf{C}_{YY} + \mathbf{R}_t)^T (\mathbf{Y}_t^o + e_{i,t} - \mathbf{Y}_{i,t}^{inf,f}) \tag{13}$$

where $\mathbf{Y}_{i,t}^{inf,f}$ contains the forecasted piezometric heads after inflation at the observation locations.

3. Synthetic Example

A synthetic bimodal confined aquifer consisting of 30% high permeability sand and 70% low permeability shale is constructed on a grid of 100 by 80 by 1 cells, each cell being 3 m by 3 m by 10 m. The SNESIM code, a multiple-point simulation program developed by Strébelle [67], is used to generate a two-facies field using the training image in Strebelle [49] (see Figure 1). Then, the facies field is populated, independently for each facies, with log-conductivity values using a sequential Gaussian simulation algorithm [48]. The parameters used in the sequential Gaussian simulations are shown in Table 1. The resulting reference log-conductivity field and its histogram are shown in Figures 2 and 3, respectively. We can see in Figure 2 that the distribution of log-conductivities is clearly non-Gaussian, and that the field has well-connected sand channels. The bimodal distribution in Figure 3 has a global mean of -0.3 ln(m/d), and a global standard deviation of 1.7 ln(m/d).

The boundary conditions used in the simulation of transient groundwater flow are: north and south boundaries, no flow; east boundary, prescribed flow as indicated in Figure 2; and west boundary, general head boundary condition with head at 2 m and leakage coefficient of 0.14 d^{-1}. The initial head is set to zero throughout the domain. Specific storage is set to 0.003 m^{-1}. The total simulation time is 500 days and it is discretized into 100 time steps. The time steps increase in size as time progresses following a geometric series with ratio 1.05. The transient flow simulator MODFLOW [e.g., 68, 69] is used as the forward model.

3.1. Scenarios

In this work, seven scenarios are used to demonstrate the power of transient piezometric head in the characterization of a bimodal hydraulic conductivity field. The impact of the covariance inflation in the characterization of the hydraulic conductivity field (see Table 2) is also analyzed. It is important to recall that no prior information about the spatial variability of conductivity is used, and that no conditioning hydraulic conductivity data are used, either.

For reference purposes, we include a Scenario S0 in the analysis. This scenario replicates the analysis performed by Zhou et al. [46], where they had information about the spatial variability of hydraulic conductivity in the form of the training images from which the reference case had been generated; therefore, the training image of Figure 1 is used to generate 1000 unconditional realizations of the two-facies distribution, which are later populated with conductivity values by Gaussian sequential simulation, in the same manner as the reference realization was built. Scenarios S1, S2, S3, S4, S5, S6 use, as initial realizations, the same 1000 homogenous fields generated based on the bimodal distribution shown in the Figure 3.

All scenarios use localization in the application of the NS-EnKF. The distance a in the localization function (Equation 9) is set to 40 m implying that correlation will be zero at a distance of 80 m. This value is chosen after analyzing the experimental cross-covariances of the first batch of realizations. Figure 4 shows the localization function. Scenarios S0, S1, S3, S5 do not use covariance inflation, whereas scenarios S2, S4, S6 do use it.

The number of observation piezometers goes from 111 down to 24 for the different scenarios as indicated next. Scenarios S1 and S2 have 111 observation piezometers (see Figure 5a), scenarios S0, S3 and S4 have 56 observation piezometers (see Figure 5b), and scenarios S5 and S6 have 24 observation piezometers (see Figure 5c). In addition, two control piezometers, not used for conditioning, are employed to verify the performance of the NS-EnKF in all the scenarios (see Figure 5). The control piezometer number 1 is located in the north-western part of the aquifer, and the control piezometer number 2 is towards the center.

4. Analysis

We have applied the localized NS-EnKF for the different scenarios described previously assimilating the piezometric observations for the first 60 time steps (67.7 days). We will show the updated log-conductivity fields after the 10th time step (2.4 days) and after the 60th time step. We will also show the piezometric evolution at the control points from time zero until the 100th time step (500 days).

Figure 6a displays the log-conductivity histogram for the initial ensemble of heterogeneous realizations used in scenario S0. Figure 6b displays the log-conductivity histogram of the updated ensemble of realizations in scenario S0 after the 60th assimilation step. Figure 7 displays at the top the log-conductivity histogram for the initial ensemble of homogeneous realizations used in scenarios S1-S6. The corresponding histograms for each scenario after the 60th assimilation step are shown in Figure 7a-7f. Comparing the updated histograms with the reference one, we can observe that the bimodality is preserved in all scenarios, although only scenarios S0, S2, S4, and S6 are able to approximately keep the original proportions between sand and shale.

Figure 8 shows the ensemble mean of the initial log-conductivity fields, together with the ensemble mean of the updated log-conductivity fields after the 10th and 60th assimilation time step for scenario S0. Similarly Figure 9 shows the ensemble variance for the same sets of log-conductivity in Figure 8.

The ensemble mean and the ensemble variance of the initial log-conductivities for scenarios S1-S6 are not shown, since they are the same as Figure 8a and Figure 9a, respectively. Figures 11 and 12 show the ensemble means of the updated fields after the 10th and 60th time step, respectively. Similarly, Figures 13 and 14 show the corresponding ensemble variances.

The initial ensemble means in Figure 8a and Figure 10a are homogeneous with a value equal to the prior mean (even for scenario S0), since the initial realizations are unconditional. For the same reason, the initial ensemble variances in Figure 9a and Figure 10b are also homogeneous with a value equal to the prior variance.

Figure 8 and Figure 9 replicate the results by Zhou et al. [46] who introduced the NS-EnKF algorithm. We can see how, as time progresses, the main channel features in the reference field are better delineated in the ensemble mean maps, and the ensemble variance decreases. Since the fastest piezometric head changes are close to the east and west boundaries, the channel features close to these boundaries can be already identified at the 10th time step. It was precisely the evolution of the ensemble mean map as a function of time seen in the these figures, what disclosed to us the importance of the transient piezometric head for hydraulic conductivity characterization. For this reason, this paper focuses in the power of assimilating transient piezometric heads using the NS-EnKF algorithm for the case in which we do not have any information about the spatial variability of hydraulic conductivities.

Figures 11a,c,e, and 12a,c,e show the ensemble means for the scenarios in which no covariance inflation has been implemented. Correspondingly, Figures 13a,c,e, and 14a,c,e show the ensemble variances for these scenarios. We notice that the implementation of the localized NS-EnKF with homogeneous initial fields results in filter inbreeding very quickly. This can be identified in the variance maps in Figures 14a,c,e, which are almost zero everywhere. Even though, after the 60th time step, some of the channel features can be identified when using 111 piezometers, we discarded these results as acceptable due to filter inbreeding. And, for this reason, we implemented covariance inflation into the localized NS-EnKF.

Figures 11b,d,f, and 12b,d,f show the ensemble means for the scenarios in which covariance inflation has been implemented. Correspondingly, Figures 13b,d,f, and 14b,d,f show the ensemble variances in these scenarios. When using 111 piezometers and covariance inflation after 60 time steps, the ensemble mean captures very well the main features of the reference field (see Figure 12b). If the number of piezometers is reduced to 56, the method can still capture the general position of the channels, but with less accuracy than in the previous case (see Figure 12d). However, if we reduce the number of piezometers down to 24, then the characterization of the channels is very poor. As in scenario S0 after 10 time steps, in scenarios S1-S6, we can start to see the appearance of the channels in the ensemble means of the updated fields. For these scenarios, in which covariance inflation was implemented, the ensemble variance after 60 time steps is too small indicating some filter inbreeding.

The issue of filter inbreeding is better analyzed by looking at the ratio of the root mean square error

($RMSE$) to the ensemble spread (ES), where $RMSE$ and ES are defined as follows:

$$RMSE = \sqrt{\frac{1}{n}\sum_{i=1}^{n}(s_i^{ref} - \langle s^a \rangle_i)^2}, \tag{14}$$

where n is the number of model elements; s_i^{ref} is the value of the reference field at node i; $\langle s^a \rangle_i$ is the ensemble mean of the updated fields, and

$$ES = \sqrt{\frac{1}{n}\sum_{i=1}^{n}\sigma_i^2}, \tag{15}$$

where σ_i is the ensemble variance of the updated fields at node i.

The $RMSE$ measures how well the ensemble average map reproduces the reference one, the smaller the $RMSE$, the better the reproduction. Yet, we know that the ensemble average map can only be a smooth representation of the spatial heterogeneity, and consequently it can never be zero. The ES measures the degree of variability across the different realizations. When ES is too close to zero, it indicates that the realizations have collapsed and filter inbreeding occurs. Liang et al. [63] show that a good way to check the degree of filter inbreeding is by analyzing the ratio of $RMSE$ to ES, which, in ideal conditions, should be 1.

Figure 15 shows the evolution of the $RMSE$ for all scenarios computed on the updated log-conductivity fields after each assimilation step. We can see how, except for S6, the $RMSE$ decreases with time. The smallest values are found for scenario S0, followed by scenario S2. Figure 16 shows the evolution with time of the ratio of $RMSE$ to ES. In this figure, we can clearly see how for scenario S0 this ratio converges quickly to 1, indicating that there is no filter inbreeding. On the other hand, filter inbreeding is very high for scenarios S1, S3, S5 (the ones without covariance inflation), and it is less pronounced for scenarios S2, S4, S6 (the ones with covariance inflation). As already noticed in Figure 12b, scenario S2 provides the best results.

Next, we analyze the reproduction of the piezometric heads at the control piezometers. Figure 17 shows the evolution of the piezometric heads at control piezometers 1 and 2 for the initial log-conductivity fields; in the top row, the evolution in the heterogeneous fields used in scenario S0, and in the bottom row, the evolution in the homogeneous fields used in the other scenarios. The figure also shows the evolution of heads in the reference field and the average of the individual realizations. Figure 18 shows the evolution at the two control points in the updated fields after 60 time steps for scenario S0. Figure 19 and Figure 20 shows the evolution of heads at control piezometers 1 and 2, respectively, in the updated fields after 60 time steps for scenarios S1-S6. Notice that for Figures 18, 19 and 20 the assimilation period lasts only until day 67.7, beyond that the log-conductivity fields are not updated anymore.

We can see in Figure 17 that with no conditioning to conductivity and without assimilating any piezometric head the spread of the responses of piezometric head is extremely large. The localized NS-EnKF with initial heterogeneous fields (scenario S0) does a good job in reducing the spread of the piezometric head curves with the conductivity fields updated up to the 60th assimilation time step. However, there is still a small bias between the reference values and the ensemble mean results.

The evolution of the piezometric heads computed on the updated fields after the 60th assimilation time step in both control piezometers is very similar for all scenarios. The spread is reduced very much with respect to the spread in the initial fields, although for some scenarios like S1, or S3, the reduction is too large due to the filter inbreeding. Scenario S2, which performed best for log-conductivity reproduction, is the one displaying the largest spread among the different realizations but also the largest bias between the reference values and the ensemble average.

In order to analyze the characterization of the log-conductivity fields in the different scenarios, we are going to perform two additional checks, one involving the advective transport of an inert solute, and the other one based on the analysis of some connectivity functions. For these checks, we will use the updated log-conductivity fields after the 60th assimilation time step.

For the transport exercise, we release 10,000 particles along an injection line at $x = 10$ m and we track them to the two control planes at $x = 100$ m and $x = 280$ m using the random walk particle tracking program RW3D [70] (see Figure 2). Porosity is assumed constant and equal to 0.3. Figure 21 shows the breakthrough curves (BTCs) corresponding to scenario S0. Figure 22 shows the BTCs at the first control plane for scenarios S1-S6, and Figure 23 shows the BTCs at the second control plane.

Again, scenario S0 is the one that performs best since the reference BTCs are within the 90% confidence interval for both control planes, and the median BTCs do an acceptable job in reproducing the reference BTCs. The non inflation scenarios display an extremely narrow 90% confidence interval, although they are able to reproduce the reference BTCs for control plane 2. Of the inflation scenarios both S2 and S4 give good results both in terms of the confidence intervals and the approximation of the reference BTC by the median. The behavior of scenario S6 is odd, particularly when compared with S5, since S5 is able to reproduce moderately well the BTCs for both control planes (with a very narrow band of uncertainty) and S6 fails completely, displaying a transport behavior much slower than in all other scenarios. This behavior must be due to the covariance inflation and the low number of conditioning points, such an inflation may result in an overall higher variability that masks the presence of the conductivity channels.

All in all, transport results could be very much dependent on the reference field used for the analysis, and should be interpreted in this view.

For the connectivity exercise, we are going to analyze the connectivity of high conductivity values in the horizontal direction. Of the different methods proposed to evaluate connectivity [e.g., 71, 72, 73], we choose the one proposed by Stauffer and Aharony [74]. Before computing the connectivity of each field we need to convert the continuous log-conductivity fields into binary fields using the indicator transform function

$$I(x) = \begin{cases} 1, & \text{if } \ln K \geq 0 \\ 0, & \text{otherwise} \end{cases} \tag{16}$$

where we chose the threshold value $\ln K = 0$ because it separates sand from shale in the reference histogram (Figure 3). The program CONNEC3D [75] computes the connectivity following the method by Stauffer and Aharony [74] as the probability that two points with log-conductivities larger than zero horizontally separated by a certain distance are connected by a continuous path of log-conductivities larger than zero. Figures 24 and 25 show the connectivity curves for the high conductivities as a function of their horizontal separation distance. Both figures show the connectivity curves computed in all realizations together with the connectivity curve computed in the reference field, and the mean of the curves. Figure 24 shows the connectivity curves for the initial heterogeneous conductivity realizations and for the updated conductivity realizations after the 60th assimilation time step for scenario S0. Figure 25 shows the connectivity functions for the updated conductivity realizations after the 60th assimilation time step for scenarios S1-S6. The connectivity functions for the initial homogeneous fields are not displayed since the connectivity in a homogeneous field is always perfect.

Analyzing Figures 24 and 25 we can arrive at the same conclusions as before. The spread of the curves for the non inflation scenarios is too small. The fact that the connectivity functions for scenarios S1 and S3 are so close to the reference connectivity function may be the explanation why the BTCs are also so well reproduced for these scenarios. Scenarios S2 and S4 show a larger spread than the non inflation scenarios, yet, the envelope of individual functions encloses the reference function, and its mean is an acceptable approximation of the reference.

5. Summary and conclusion

In this paper we wanted to show the power of transient piezometric head information for the characterization of the spatial variability of hydraulic conductivity, for hydraulic conductivity fields displaying spatial patterns that can not be characterized with multi-Gaussian approaches. We have taken an extreme position in that we assume that we do not have any information about hydraulic conductivity, neither locally nor globally, except for its bimodal marginal distribution. Zhou et al. [46] already showed that transient piezometric head was enough for hydraulic conductivity characterization if a training image for the hydraulic conductivity was available. Our main finding is that without such a training image but with enough transient piezometric head information, we can generate an ensemble of realizations that captures the main patterns of the non-Gaussian reference field. The number of piezometers below which the characterization will deteriorate is very much problem dependent; both the type of underlying conductivity field and the boundary conditions of the flow problem will have an impact on how many piezometers are necessary and for how long they have to be measured. In this paper we do not seek to give an answer to this latter question, but rather emphasize that even for a clearly channelized bimodal conductivity field, the transient piezometric heads carry very valuable information about the conductivity spatial heterogeneity, and therefore, we should always do every attempt to try to assimilate these data into our flow models. On occasions, piezometric head is disregarded for the purpose of inverse modeling on the account that it is a low pass filter of the conductivities, it is true that in the examples shown, the assimilation of piezometric head cannot get the short scale variability of the reference field, but the main patterns are clearly identified. We took a rather radical approach, i.e., no spatial information was used. However, additional information about the patterns in conductivity, without the need of resorting to a training image, such as the main orientation of the channels and their width, will help improving the characterization. If in addition, a training image is available, the characterization would improve as demonstrated in the reference scenario S0.

We have also shown that filter inbreeding can be reduced with covariance inflation techniques. Although, when no inbreeding appears, as in scenario S0, there is no need for such an inflation.

We conclude that the NS-EnKF approach developed by Zhou et al. [46] proves again capable of preserving the bimodality of the reference field, even for the case in which there is very limited information about the log-conductivities. Covariance localization and inflation are necessary to reduce filter inbreeding. For the specific case analyzed in this paper, 56 piezometers were enough to capture the main channels in the reference field; however, our purpose is not to give a rule about how many piezometers are needed, but rather to emphasize the importance of accounting for transient piezometric heads in our inverse modeling.

Acknowledgements The first author acknowledges the financial support from the China Scholarship Council (CSC). Financial support to carry out this work was also received from the Spanish Ministry of Science and Innovation through project CGL2011-23295.

References

[1] Li, L., Zhou, H., Franssen, H., Gómez-Hernández, J.. Groundwater flow inverse modeling in non-multigaussian media: performance assessment of the normal-score ensemble kalman filter. Hydrol Earth Syst Sci Discuss 2011;8(4):6749–88.

[2] Capilla, J., Llopis-Albert, C.. Gradual conditioning of non-gaussian transmissivity fields to flow and mass transport data: 1. theory. Journal of Hydrology 2009;371(1):66–74.

[3] Hu, L.. Gradual deformation and iterative calibration of gaussian-related stochastic models. Mathematical Geology 2000;32(1):87–108.

[4] Gómez-Hernánez, J., Sahuquillo, A., Capilla, J.. Stochastic simulation of transmissivity fields conditional to both transmissivity and piezometric data–1. theory. Journal of Hydrology(Amsterdam) 1997;203(1):167–74.

[5] Fu, J., Jaime Gómez-Hernández, J.. Uncertainty assessment and data worth in groundwater flow and mass transport modeling using a blocking markov chain monte carlo method. Journal of Hydrology 2009;364(3):328–41.

[6] Oliver, D., Cunha, L., Reynolds, A.. Markov chain monte carlo methods for conditioning a permeability field to pressure data. Mathematical Geology 1997;29(1):61–91.

[7] Alcolea, A., Carrera, J., Medina, A.. Pilot points method incorporating prior information for solving the groundwater flow inverse problem. Advances in Water Resources 2006;29(11):1678–89.

[8] Wen, X., Deutsch, C., Cullick, A.. Construction of geostatistical aquifer models integrating dynamic flow and tracer data using inverse technique. Journal of Hydrology 2002;255(1):151–68.

[9] RamaRao, B., LaVenue, A., De Marsily, G., Marietta, M.. Pilot point methodology for automated calibration of an ensemble of conditionally simulated transmissivity fields: 1. theory and computational experiments. Water Resources Research 1995;31(3):475–93.

[10] Franssen, H., Gómez-Hernández, J., Sahuquillo, A.. Coupled inverse modelling of groundwater flow and mass transport and the worth of concentration data. Journal of Hydrology 2003;281(4):281–95.

[11] Franssen, H., Kinzelbach, W.. Real-time groundwater flow modeling with the ensemble kalman filter: Joint estimation of states and parameters and the filter inbreeding problem. Water Resources Research 2008;44(9):W09408.

[12] Aanonsen, S., Nævdal, G., Oliver, D., Reynolds, A., Vallès, B.. The ensemble kalman filter in reservoir engineering–a review. SPE Journal 2009;14(3):393–412.

[13] Chen, Y., Zhang, D.. Data assimilation for transient flow in geologic formations via ensemble kalman filter. Advances in Water Resources 2006;29(8):1107–22.

[14] Evensen, G.. The ensemble kalman filter: Theoretical formulation and practical implementation. Ocean dynamics 2003;53(4):343–67.

[15] Moradkhani, H., Sorooshian, S., Gupta, H., Houser, P.. Dual state–parameter estimation of hydrological models using ensemble kalman filter. Advances in Water Resources 2005;28(2):135–47.

[16] Dowell, D., Zhang, F., Wicker, L., Snyder, C., Crook, N.. Wind and temperature retrievals in the 17 may 1981 arcadia, oklahoma, supercell: Ensemble kalman filter experiments 2010;.

[17] Bertino, L., Evensen, G., Wackernagel, H.. Sequential data assimilation techniques in oceanography. International Statistical Review 2003;71(2):223–41.

[18] Li, L., Zhou, H., Gómez-Hernández, J., Hendricks Franssen, H.. Jointly mapping hydraulic conductivity and porosity by assimilating concentration data via ensemble kalman filter. Journal of Hydrology 2012;.

[19] Sun, A., Morris, A., Mohanty, S.. Sequential updating of multimodal hydrogeologic parameter fields using localization and clustering techniques. Water Resources Research 2009;45(7):W07424.

[20] Simon, E., Bertino, L.. Application of the gaussian anamorphosis to assimilation in a 3-d coupled physical-ecosystem model of the north atlantic with the enkf: a twin experiment. Ocean Sci 2009;5(4):495–510.

[21] Chen, Y., Oliver, D., Zhang, D.. Data assimilation for nonlinear problems by ensemble kalman filter with reparameterization. Journal of Petroleum Science and Engineering 2009;66(1):1–14.

[22] Gordon, N., Salmond, D., Smith, A.. Novel approach to nonlinear/non-gaussian bayesian state estimation. In: Radar and Signal Processing, IEE Proceedings F; vol. 140. IET; 1993, p. 107–13.

[23] Losa, S., Kivman, G., Schröter, J., Wenzel, M.. Sequential weak constraint parameter estimation in an ecosystem model. Journal of Marine Systems 2003;43(1):31–49.

[24] Van Leeuwen, P.. Particle filtering in geophysical systems. Monthly Weather Review 2009;137(12):4089–114.

[25] Schöniger, A., Nowak, W., Franssen, H.. Parameter estimation by ensemble kalman filters with transformed data: Approach and application to hydraulic tomography. Water Resources Research 2012;48(4):W04502.

[26] Apte, A., Hairer, M., Stuart, A., Voss, J.. Sampling the posterior: An approach to non-gaussian data assimilation. Physica D: Nonlinear Phenomena 2007;230(1):50–64.

[27] Chen, R., Liu, J.. Mixture kalman filters. Journal of the Royal Statistical Society: Series B (Statistical Methodology) 2000;62(3):493–508.

[28] Dovera, L., Della Rossa, E.. Multimodal ensemble kalman filtering using gaussian mixture models. Computational Geosciences 2011;15(2):307–23.

[29] Reich, S.. A gaussian-mixture ensemble transform filter. Quarterly Journal of the Royal Meteorological Society 2011;138(662):222–33.

[30] Stordal, A., Karlsen, H., Nævdal, G., Skaug, H., Vallès, B.. Bridging the ensemble kalman filter and particle filters: the adaptive gaussian mixture filter. Computational Geosciences 2011;15(2):293–305.

[31] Chen, Y., Oliver, D.. Parameterization techniques to improve mass conservation and data assimilation for ensemble kalman filter. In: SPE Western Regional Meeting. 2010,.

[32] Chang, H., Zhang, D., Lu, Z.. History matching of facies distribution with the enkf and level set parameterization. Journal of Computational Physics 2010;229(20):8011–30.

[33] Li, X., Lei, Z., White, C., Allen, G., Qin, G., Tsai, F.. Grid-enabled ensemble subsurface modeling. In: Proceedings of The 19th IASTED International Conference on Parallel and Distributed Computing and Systems (PDCS 2007). 2007,.

[34] Liu, N., Oliver, D.. Critical evaluation of the ensemble kalman filter on history matching of geologic facies. In: SPE Reservoir Simulation Symposium. 2005,.

[35] Gu, Y., Oliver, D.. An iterative ensemble kalman filter for multiphase fluid flow data assimilation. SPE Journal 2007;12(4):438–46.

[36] Gu, Y., Oliver, D.. The ensemble kalman filter for continuous updating of reservoir simulation models. TRANSACTIONS-AMERICAN SOCIETY OF MECHANICAL ENGINEERS JOURNAL OF ENERGY RESOURCES TECHNOLOGY 2006;128(1):79.

[37] Wen, X., Chen, W.. Some practical issues on real-time reservoir model updating using ensemble kalman filter. In: International Petroleum Technology Conference. 2005,.

[38] Wen, X., Chen, W.. Real-time reservoir model updating using ensemble kalman filter with confirming option. SPE Journal 2006;11(4):431–42.

[39] Li, G., Reynolds, A.. An iterative ensemble kalman filter for data assimilation. In: SPE Annual Technical Conference and Exhibition. 2007,.

[40] Wang, Y., Li, G., Reynolds, A.. Estimation of depths of fluid contacts by history matching using iterative ensemble-kalman smoothers. SPE Journal 2010;15(2):509–25.

[41] Zhao, Y., Reynolds, A., Li, G.. Generating facies maps by assimilating production data and seismic data with the ensemble kalman filter. In: SPE/DOE Symposium on Improved Oil Recovery. 2008,.

[42] Simon, E., Bertino, L.. Gaussian anamorphosis extension of the denkf for combined state parameter estimation: Application to a 1d ocean ecosystem model. Journal of Marine Systems 2012;89(1):1–18.

[43] Bertino, L., Hollard, A., Evensen, G., Wackernagel, H.. An ensemble kalman filter for non-gaussian variables. In: EGS-AGU-EUG Joint Assembly; vol. 1. 2003, p. 5171.

[44] Bocquet, M., Pires, C., Wu, L.. Beyond gaussian statistical modeling in geophysical data assimilation. Monthly Weather Review 2010;138(8):2997–3023.

[45] Béal, D., Brasseur, P., Brankart, J., Ourmières, Y., Verron, J., et al. Characterization of mixing errors in a coupled physical biogeochemical model of the north atlantic: implications for nonlinear estimation using gaussian anamorphosis. Ocean Science 2010;(6).

[46] Zhou, H., Gómez-Hernández, J., Hendricks Franssen, H., Li, L.. An approach to handling non-gaussianity of parameters and state variables in ensemble kalman filtering. Advances in Water Resources 2011;34(7):844–64.

[47] Li, L., Zhou, H., Hendricks Franssen, H., Gómez-Hernández, J.. Groundwater flow inverse modeling in non-multigaussian media: performance assessment of the normal-score ensemble kalman filter. Hydrology and Earth System Sciences 2012;16(2):573.

[48] Gómez-Hernández, J.J., Journel, A.G.. Joint sequential simulation of multi-Gaussian fields. Geostatistics Troia 1993;92(1):85–94.

[49] Strebelle, S.. Conditional simulation of complex geological structures using multiple-point statistics. Mathematical Geology 2002;34(1):1–21.

[50] Mariethoz, G., Renard, P., Straubhaar, J.. The direct sampling method to perform multiple-point geostatistical simulations. Water Resources Research 2010;46(11):W11536.

[51] Deutsch, C.V., Journel, A.G.. GSLIB, Geostatistical Software Library and User's Guide. New York: Oxford University Press; second ed.; 1998.

[52] Zhou, H., Li, L., Hendricks Franssen, H., Gómez-Hernández, J.. Pattern recognition in a bimodal aquifer using the normal-score ensemble kalman filter. Mathematical Geosciences 2012;:1–17.

[53] Xu, T., Jaime Gómez-Hernández, J., Li, L., Zhou, H.. Parallelized ensemble kalman filter for hydraulic conductivity characterization. Computers & Geosciences 2013;52:42–9.

[54] Chen, Y., Oliver, D.. Cross-covariances and localization for enkf in multiphase flow data assimilation. Computational Geosciences 2010;14(4):579–601.

[55] Greybush, S., Kalnay, E., Miyoshi, T., Ide, K., Hunt, B.. Balance and ensemble kalman filter localization techniques. Monthly Weather Review 2011;139(2):511–22.

[56] Houtekamer, P., Mitchell, H.. A sequential ensemble kalman filter for atmospheric data assimilation. Monthly Weather Review 2001;129(1):123–37.

[57] Bergemann, K., Reich, S.. A localization technique for ensemble kalman filters. Quarterly Journal of the Royal Meteorological Society 2010;136(648):701–07.

[58] Nan, T., Wu, J.. Groundwater parameter estimation using the ensemble kalman filter with localization. Hydrogeology Journal 2011;19(3):547–61.

[59] GASPARI, G.. Construction of correlation functions in two and three dimensions. Quart J Roy Meteor Soc 1999;125:723–57.

[60] Hamill, T., Whitaker, J., Snyder, C.. Distance-dependent filtering of background error covariance estimates in an ensemble kalman filter. Monthly Weather Review 2001;129(11):2776–90.

[61] Anderson, J.. An adaptive covariance inflation error correction algorithm for ensemble filters. Tellus A 2007;59(2):210–24.

[62] Zheng, X.. An adaptive estimation of forecast error covariance parameters for kalman filtering data assimilation. Advances in Atmospheric Sciences 2009;26(1):154–60.

[63] Liang, X., Zheng, X., Zhang, S., Wu, G., Dai, Y., Li, Y.. Maximum likelihood estimation of inflation factors on error covariance matrices for ensemble kalman filter assimilation. Quarterly Journal of the Royal Meteorological Society 2011;138(662):263–73.

[64] Li, H., Kalnay, E., Miyoshi, T.. Simultaneous estimation of covariance inflation and observation errors within an ensemble kalman filter. Quarterly Journal of the Royal Meteorological Society 2009;135(639):523–33.

[65] Kurtz, A., Lugolobi, F., Salvucci, G.. Germanium-silicon as a flow path tracer: Application to the rio icacos watershed. Water Resources Research 2011;47(6):W06516.

[66] Wang, X., Bishop, C.. A comparison of breeding and ensemble transform kalman filter ensemble forecast schemes. Journal of the atmospheric sciences 2003;60(9):1140–58.

[67] Strébelle, S.. Sequential simulation drawing structures from training images. Ph.D. thesis; Stanford University. 187pp; 2000.

[68] McDonald, M., Harbaugh, A.. A modular three-dimensional finite-difference ground-water flow model. Scientific Publications Company; 1984.

[69] Harbaugh, A., et al. MODFLOW-2000, the US Geological Survey modular ground-water model: User guide to modularization concepts and the ground-water flow process. US Geological Survey; 2000.

[70] Fernàndez-Garcia, D., Illangasekare, T., Rajaram, H.. Differences in the scale dependence of dispersivity and retardation factors estimated from forced-gradient and uniform flow tracer tests in three-dimensional physically and chemically heterogeneous porous media. Water resources research 2005;41(3):W03012.

[71] Western, A., Blöschl, G., Grayson, R.. Toward capturing hydrologically significant connectivity in spatial patterns. Water Resources Research 2001;37(1):83–97.

[72] Knudby, C., Carrera, J.. On the relationship between indicators of geostatistical, flow and transport connectivity. Advances in Water Resources 2005;28(4):405–21.

[73] Neuweiler, I., Cirpka, O.. Homogenization of richards equation in permeability fields with different connectivities. Water resources research 2005;41(2):W02009.

[74] Stauffer, D., Aharony, A.. Introduction to percolation theory. Taylor and Francis, London. 181pp; 1994.

[75] Pardo-Igúzquiza, E., Dowd, P.. Connec3d: a computer program for connectivity analysis of 3d random set models. Computers & geosciences 2003;29(6):775–85.

Table 1: Parameters of the random functions describing the spatial continuity of the sand and shale logconductivities

Facies	Proportion	Mean [ln [m/d]]	Std.dev [ln [m/d]]	Variogram type	λ_x [m]	λ_y [m]	sill
Sand	0.3	2.1	0.7	exponential	144	72	1
Shale	0.7	-1.4	0.7	exponential	72	72	0.35

Table 2: Definition of scenarios

Scenario	S0	S1	S2	S3	S4	S5	S6
Initial Homogenous fields		$\surd$	$\surd$	$\surd$	$\surd$	$\surd$	$\surd$
Initial Heterogenous fields	$\surd$						
Observation piezometers (111)		$\surd$	$\surd$				
Observation piezometers (56)	$\surd$			$\surd$	$\surd$		
Observation piezometers (24)						$\surd$	$\surd$
No variance inflation	$\surd$	$\surd$		$\surd$		$\surd$	
Variance inflation			$\surd$		$\surd$		$\surd$

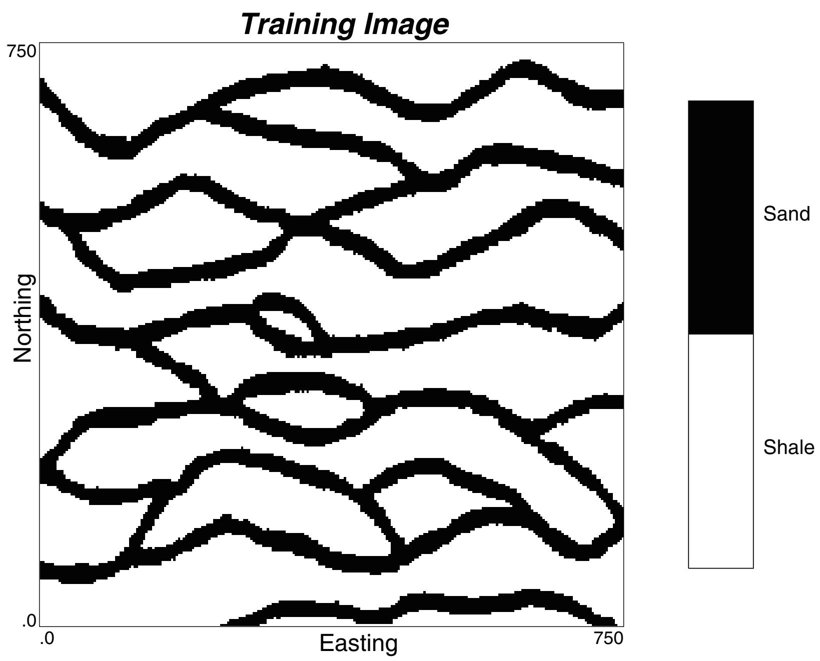

Figure 1: Training image used to generate the ensemble of binary facies realizations.

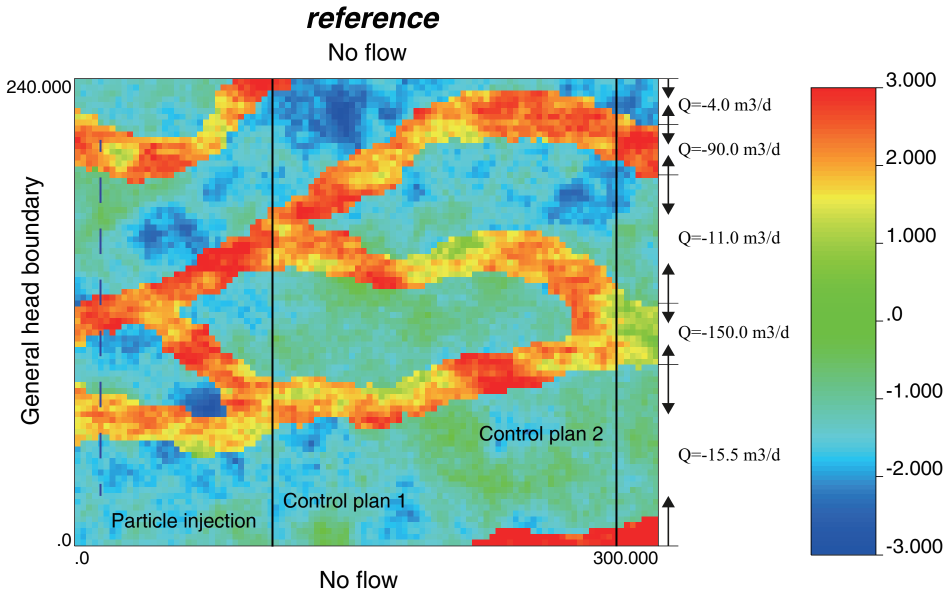

Figure 2: Reference field. The line source where particles are injected is shown with the blue dashed line, the two control planes indicated by the black lines are used to compute breakthrough curves.

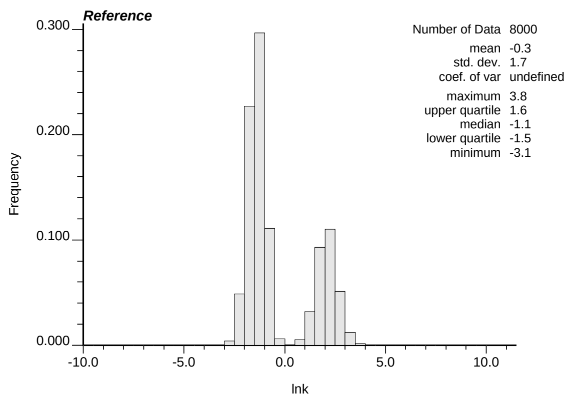

Figure 3: The histogram of the reference field

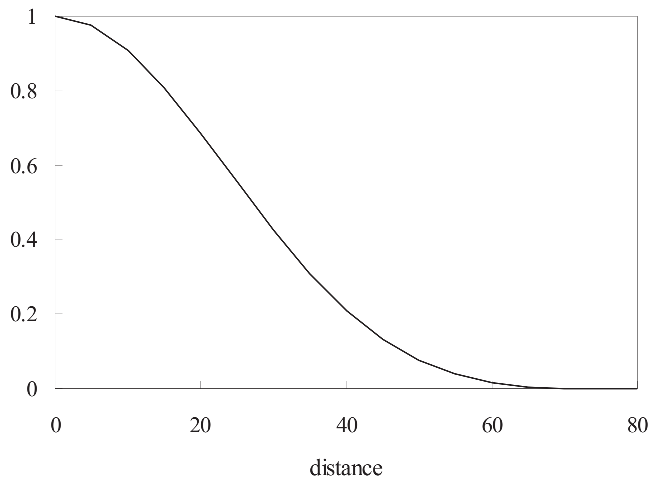

Figure 4: The localization function

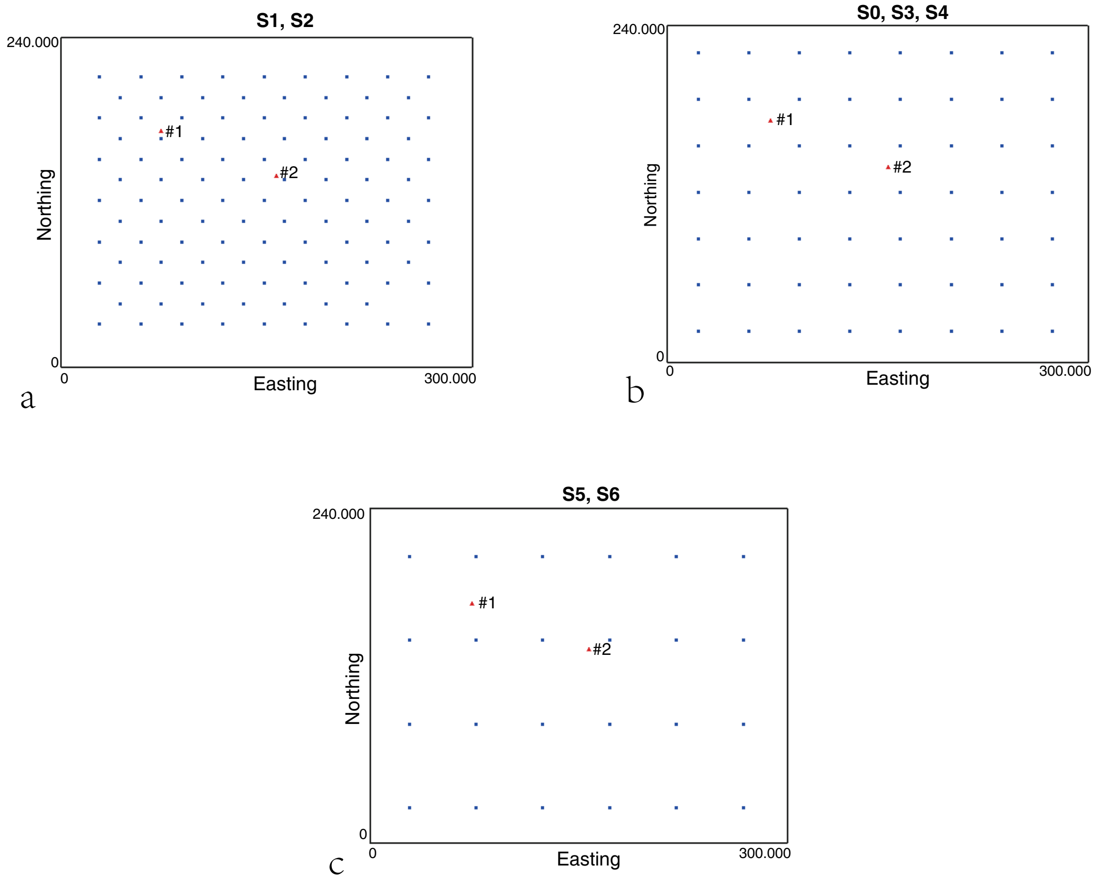

Figure 5: Graphs a,b,c show the locations of the 111, 56, 24 observation piezometers, respectively. The blue squares denote observation piezometers, and the red triangles, control piezometers.

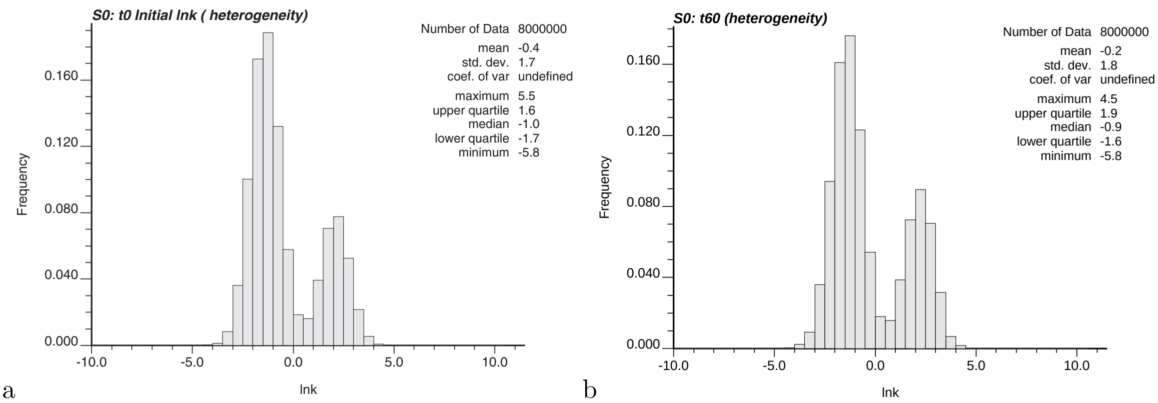

Figure 6: Scenario S0. Log-conductivity histograms for the initial ensemble of realizations and for the updated ensemble of realizations after the 60th assimilation step.

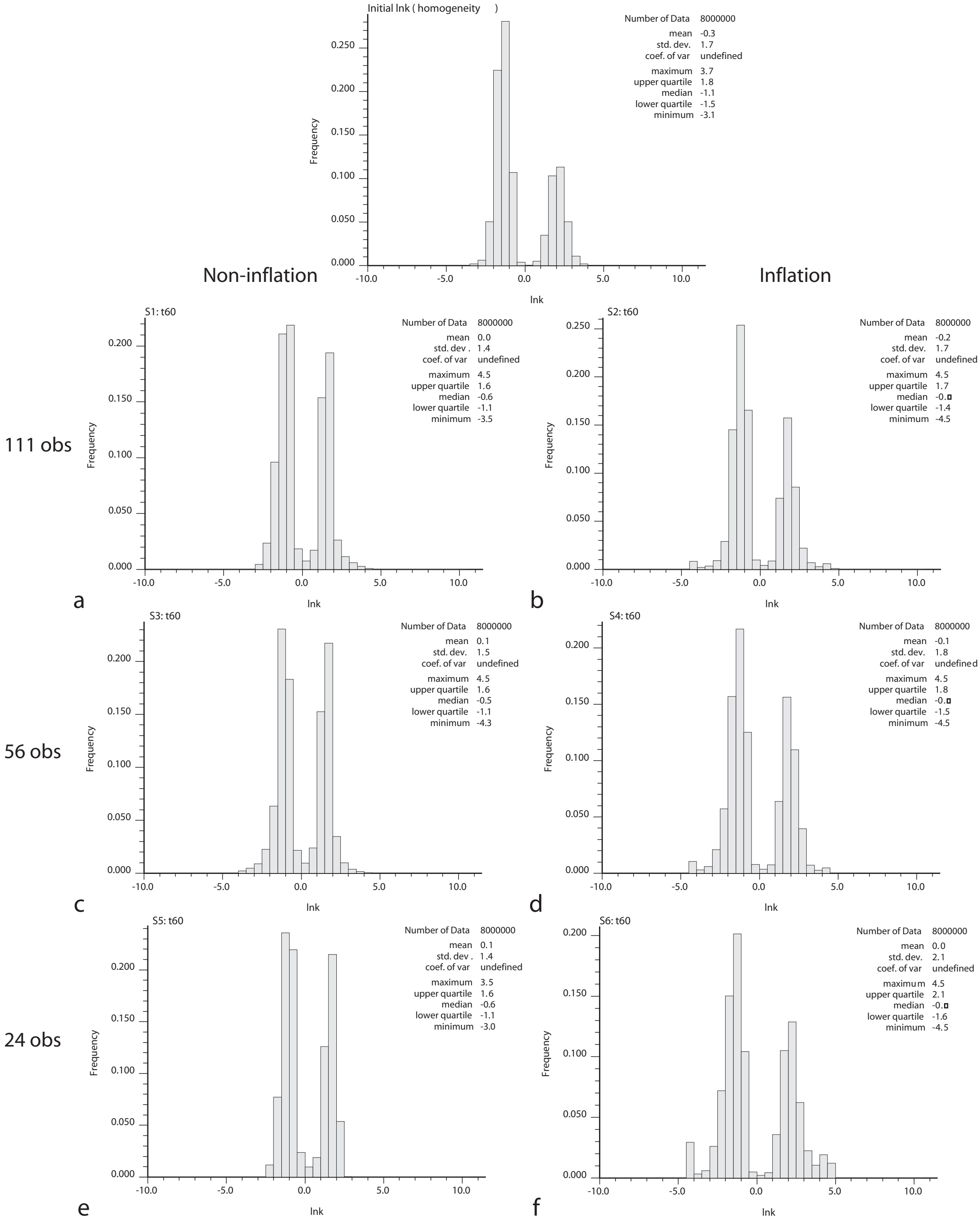

Figure 7: Scenarios S1-S6. Log-conductivity histograms. The top one shows the histogram for the initial ensemble of homogeneous realizations used in scenarios S1-S6; graphs a to f show the histograms for the corresponding scenarios after the 60th data assimilation step. The scenarios without covariance inflation are shown in the left column; the scenarios with covariance inflation are shown in the right column. The number of observation piezometers used is indicated in the left.

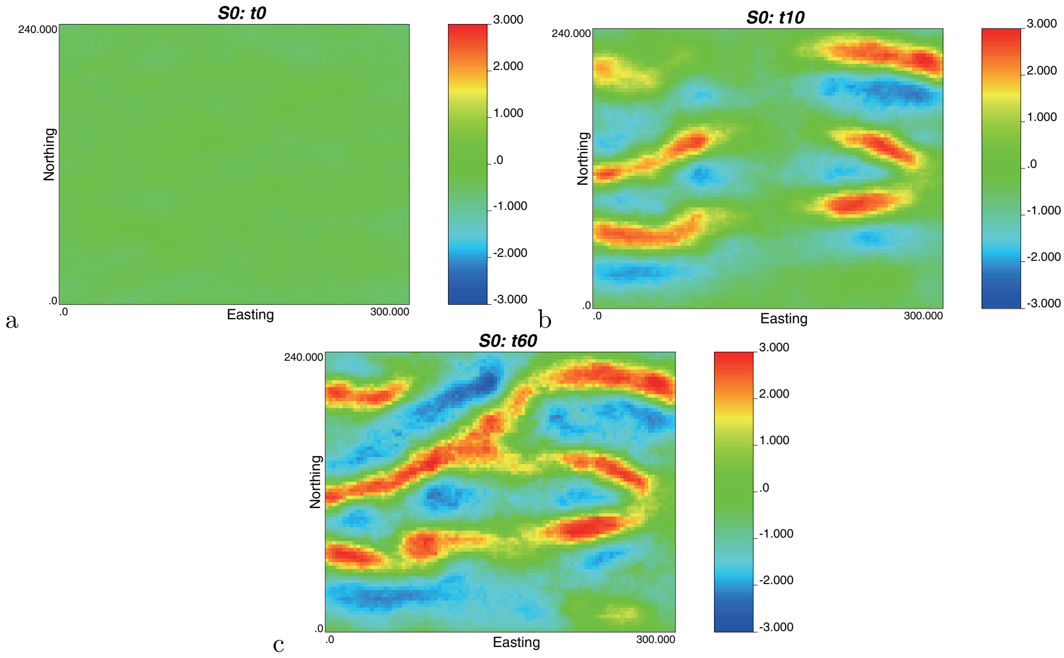

Figure 8: Scenario S0. Ensemble mean of $\ln K$ for the initial realizations and after assimilating heads at the 10th and 60th time steps.

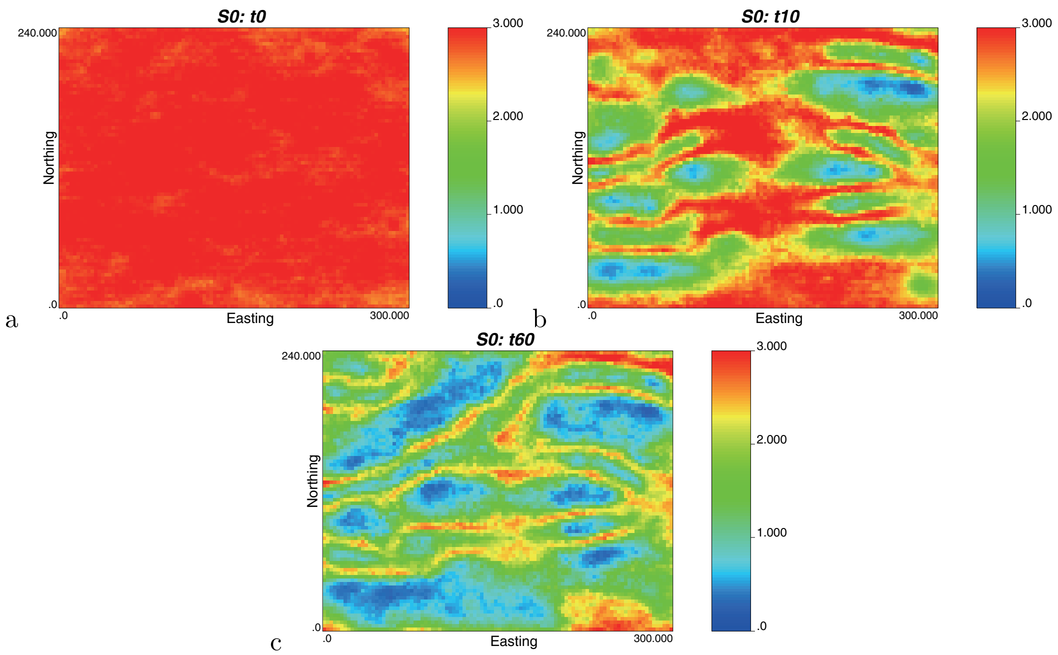

Figure 9: Scenario S0. Ensemble $\ln K$ variance for the initial realizations and after assimilating heads at the 10th and 60th time steps.

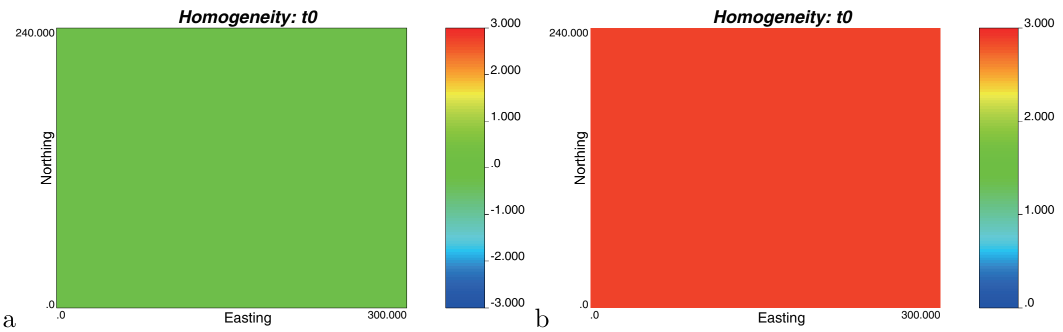

Figure 10: Maps a,b show the ensemble mean and ensemble variance of the initial realizations for the scenarios with initial homogenous fields (S1-S6).

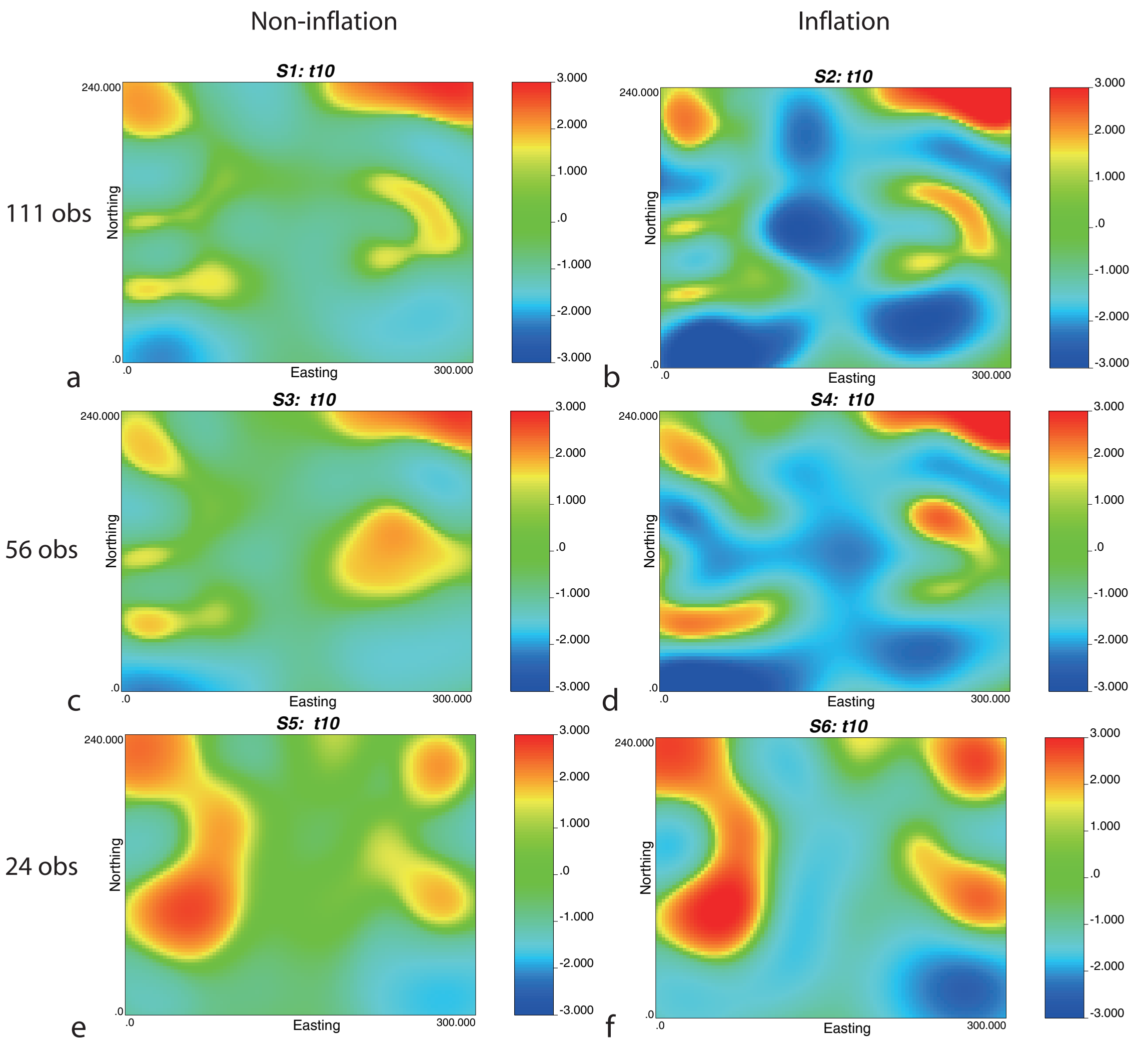

Figure 11: Scenarios S1-S6. Log-conductivity ensemble mean computed after the 10th time step.

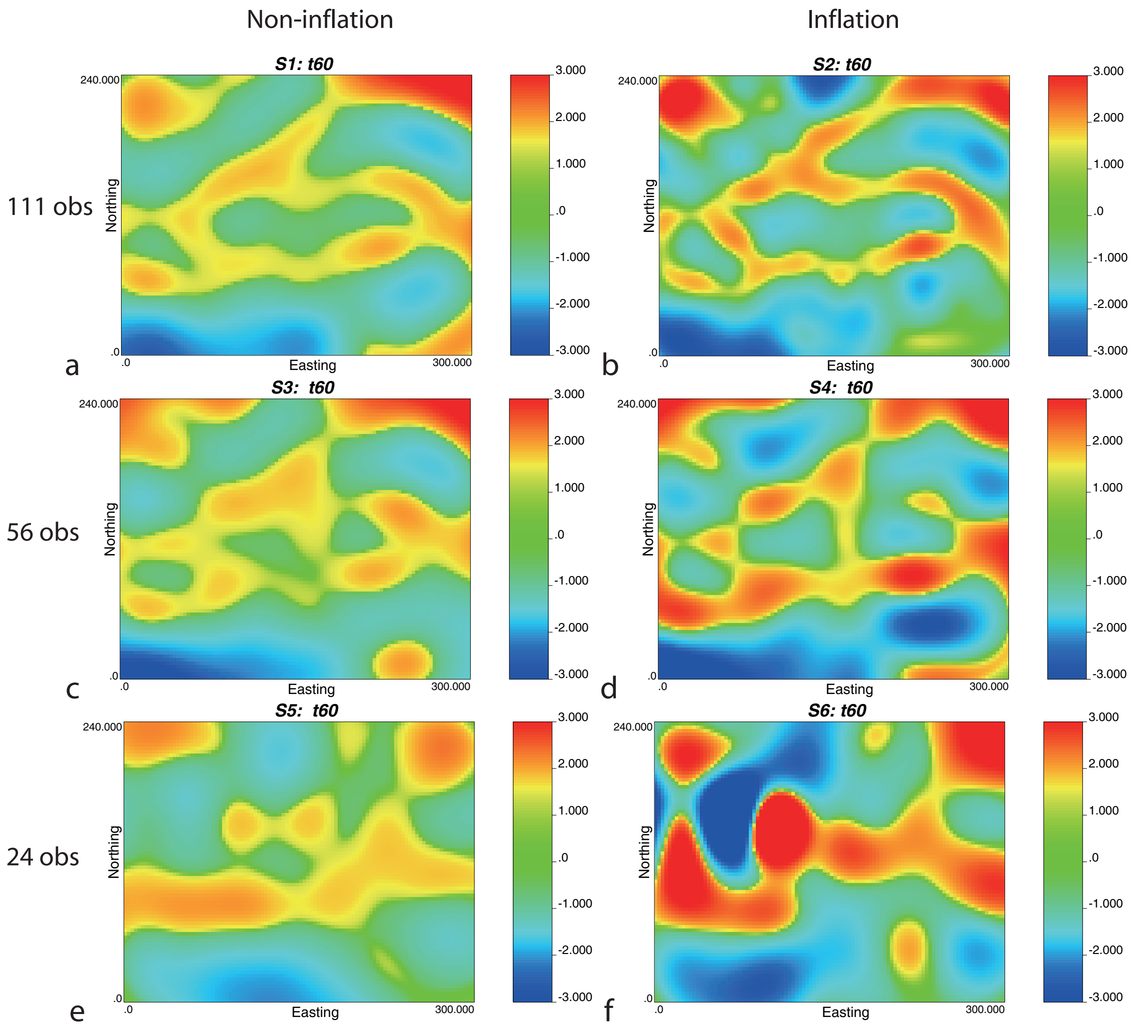

Figure 12: Scenarios S1-S6. Log-conductivity ensemble mean computed after the 60th time step.

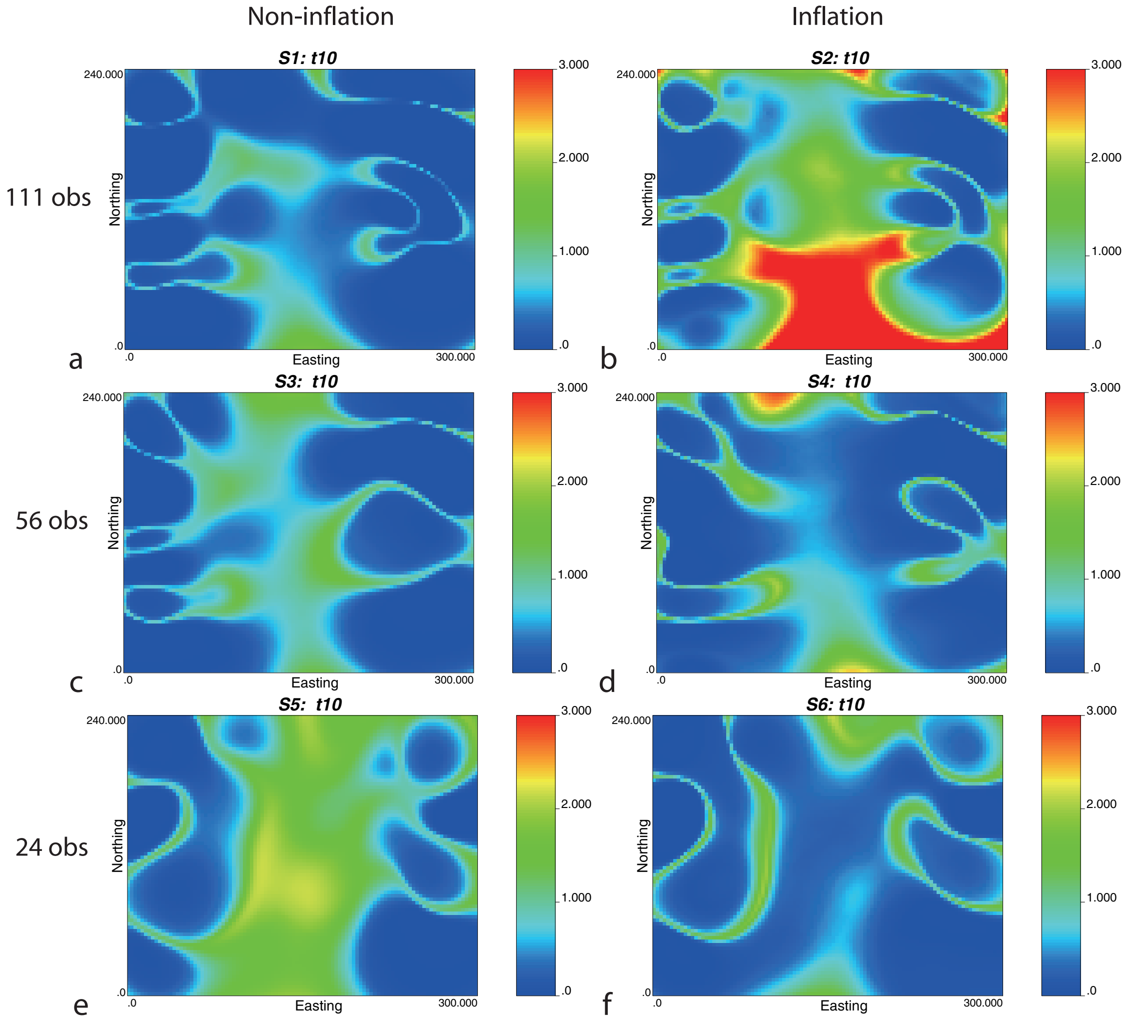

Figure 13: Scenarios S1-S6. Log-conductivity ensemble variance computed after the 10th time step.

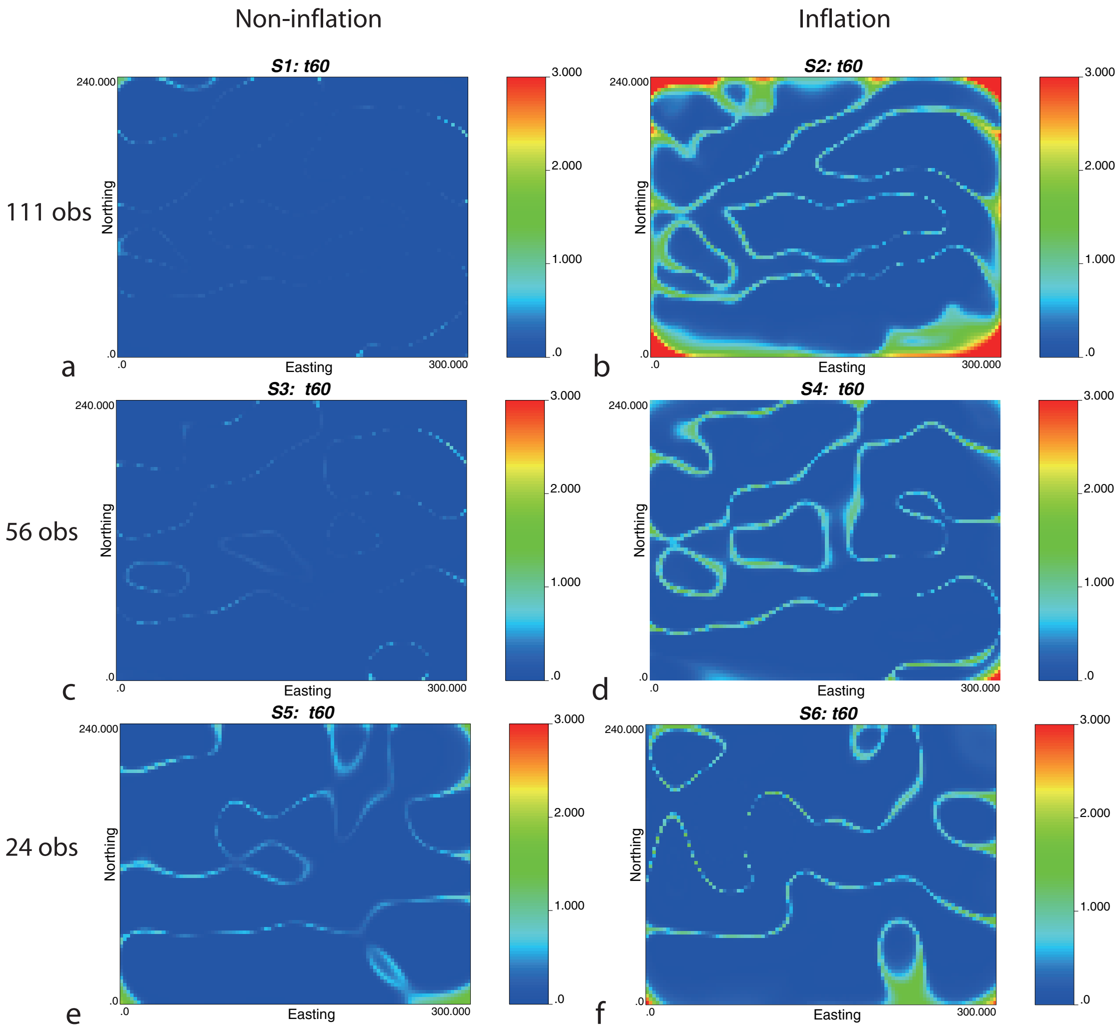

Figure 14: Scenarios S1-S6. Log-conductivity ensemble variance computed after the 60th time step.

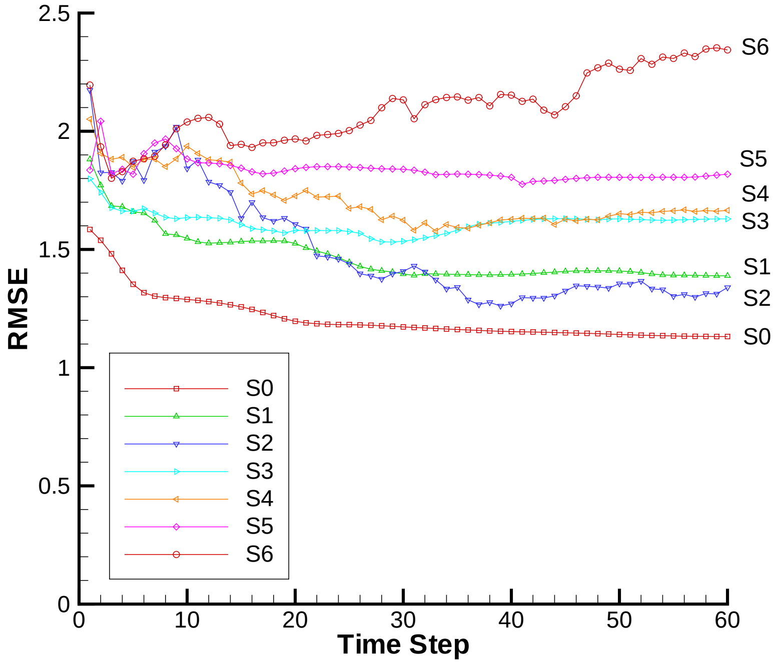

a

Figure 15: $RMSE$

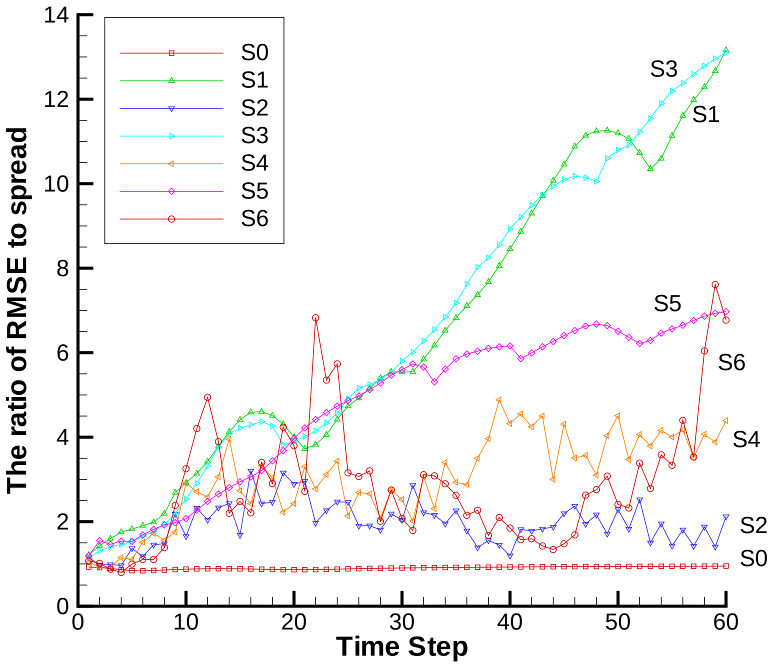

a

Figure 16: The ratio of $RMSE$ to SE

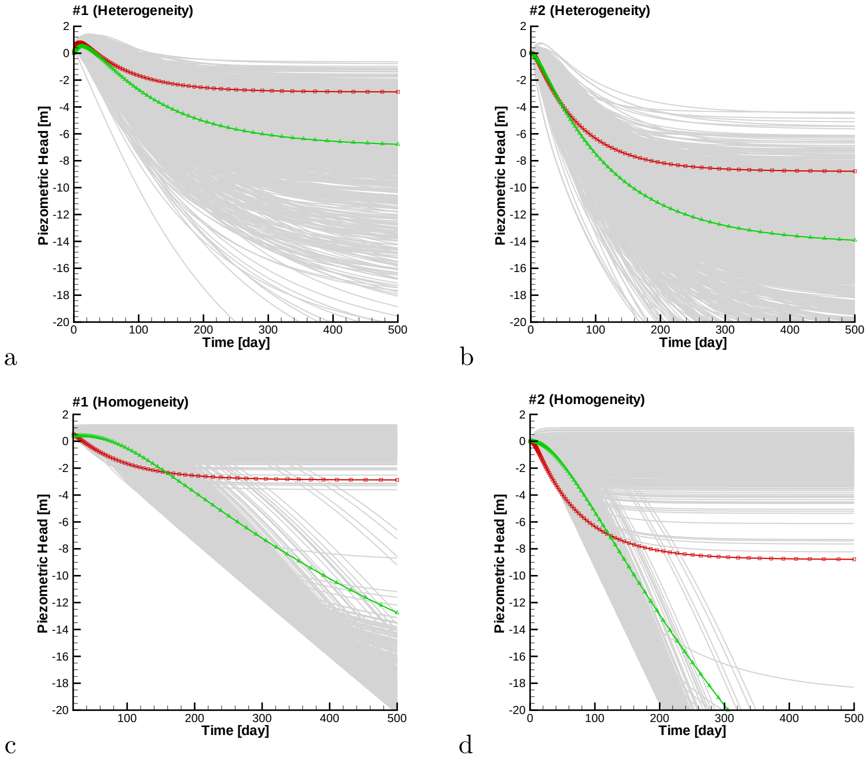

Figure 17: Graphs a,b show the piezometric head time evolution of the initial ensemble of heterogenous log-conductivity realizations at the control piezometers 1 and 2, respectively; graphs c,d show the piezometric head time evolution on the initial homogenous realizations at the two control piezometers. The red square line corresponds to the piezometric head time evolution in the reference, the green triangle line corresponds to the mean of the ensemble, and the gray lines correspond to the realizations.

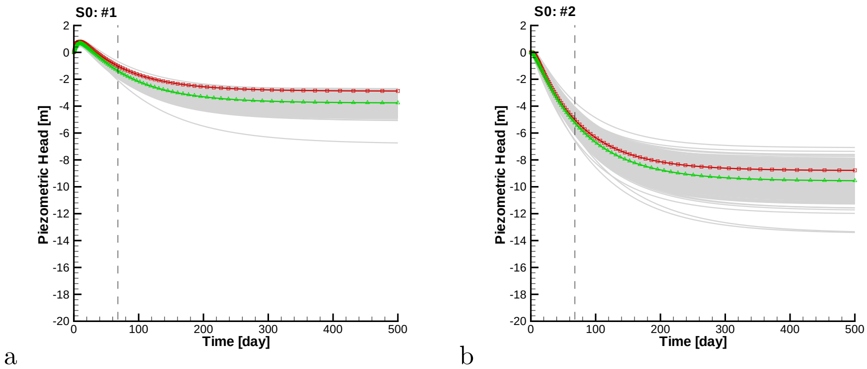

Figure 18: Scenario S0. The piezometric head time evolution after the 60th time step for the two control piezometers. The red square line corresponds to the piezometric head time evolution in the reference, the green delta line corresponds to the mean of the ensemble, the gray lines correspond to the realizations and the vertical dashed lines indicate the conditioning period.

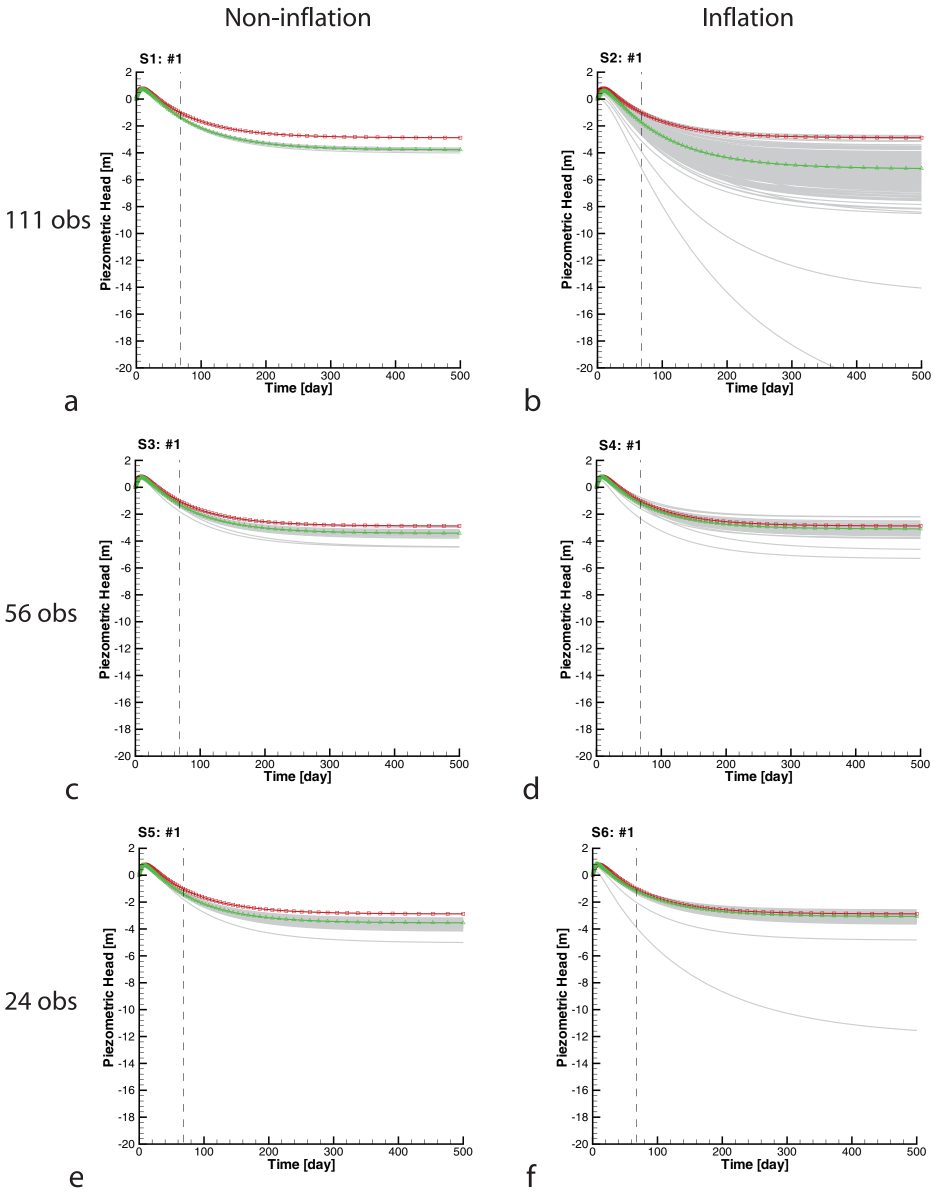

Figure 19: Scenarios S1-S6. The piezometric head time evolution at the control piezometer 1 after the 60th time step. The red square line corresponds to the piezometric head time evolution in the reference, the green delta line corresponds to the mean of the ensemble, the gray lines correspond to the realizations and the vertical dashed lines indicate the conditioning period.

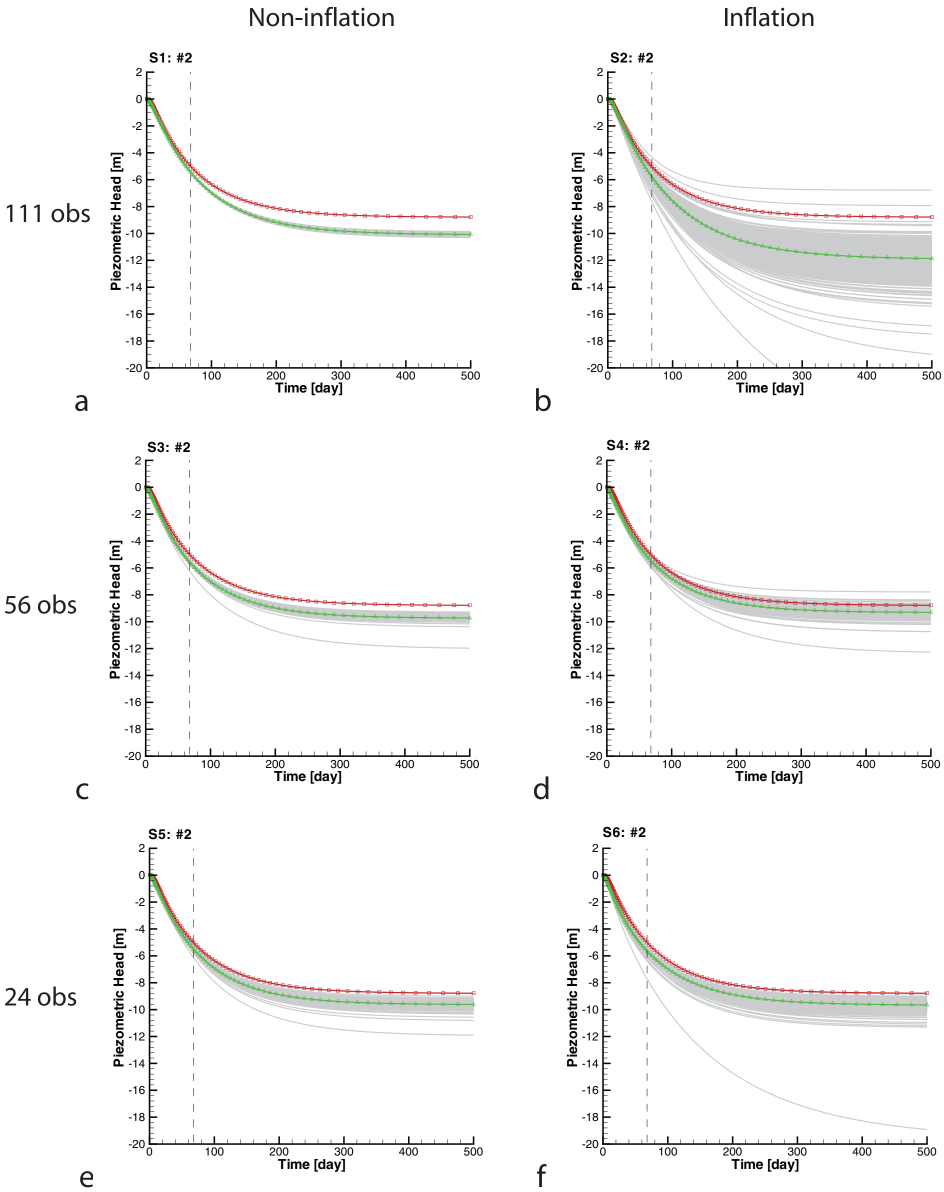

Figure 20: Scenarios S1-S6. The piezometric head time evolution at the control piezometer 2 after the 60th time step. The red square line corresponds to the piezometric head time evolution in the reference, the green delta line corresponds to the mean of the ensemble, the gray lines correspond to the realizations and the vertical dashed lines indicate the conditioning period.

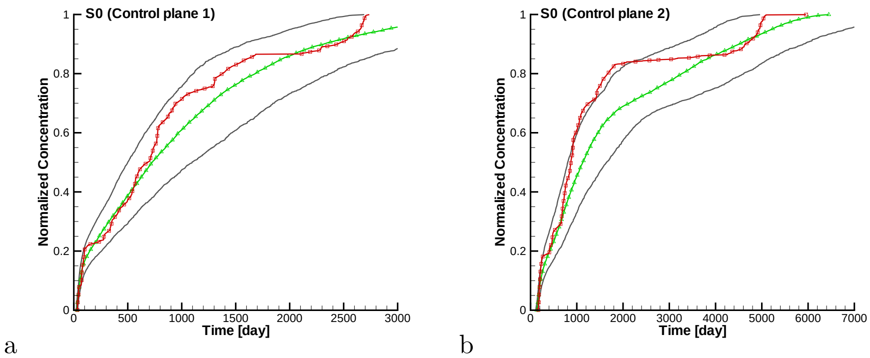

Figure 21: Graphs a,b show the BTCs at the two control planes for scenario S0. The red square line corresponds to BTCs in the reference. The black lines correspond to the 5 and 95 percentiles of all realization BTCs, and the green delta line corresponds to the median.

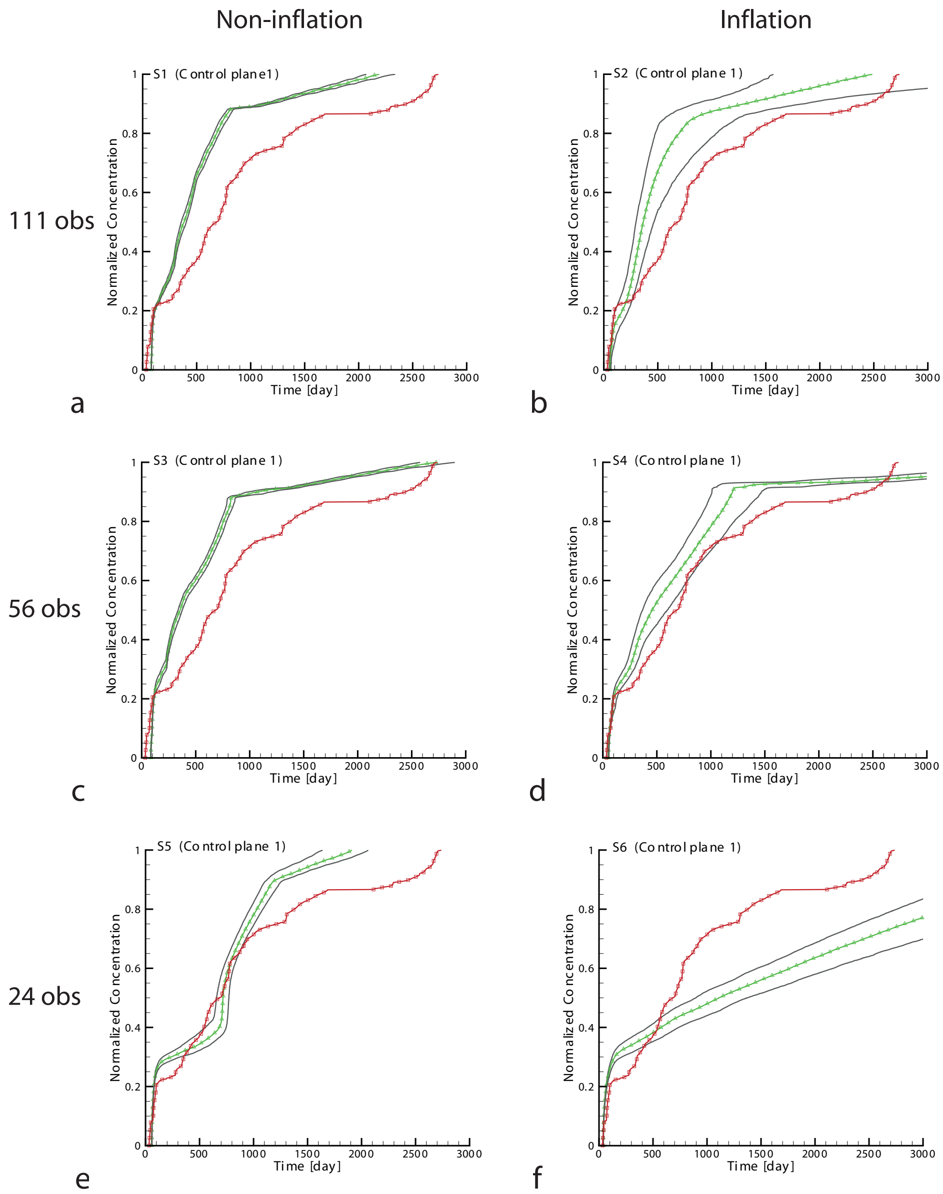

Figure 22: Scenarios S1-S6. The BTCs at the first control plane. The red square line corresponds to BTCs in the reference. The black lines correspond to the 5 and 95 percentiles of all realization BTCs, and the green delta line corresponds to the median.

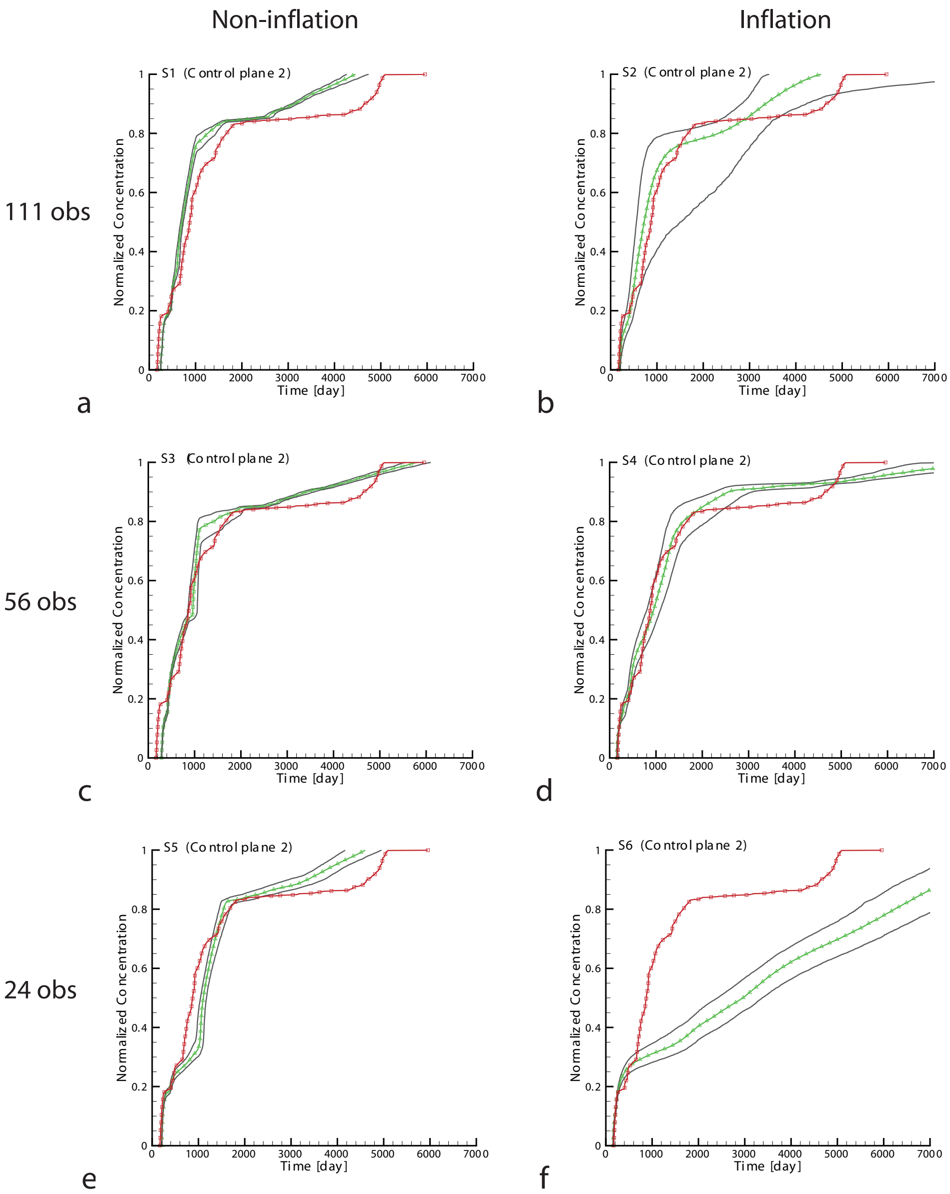

Figure 23: Scenarios S1-S6. The BTCs at the second control plane. The red square line corresponds to BTCs in the reference. The black lines correspond to the 5 and 95 percentiles of all realization BTCs, and the green delta line corresponds to the median.

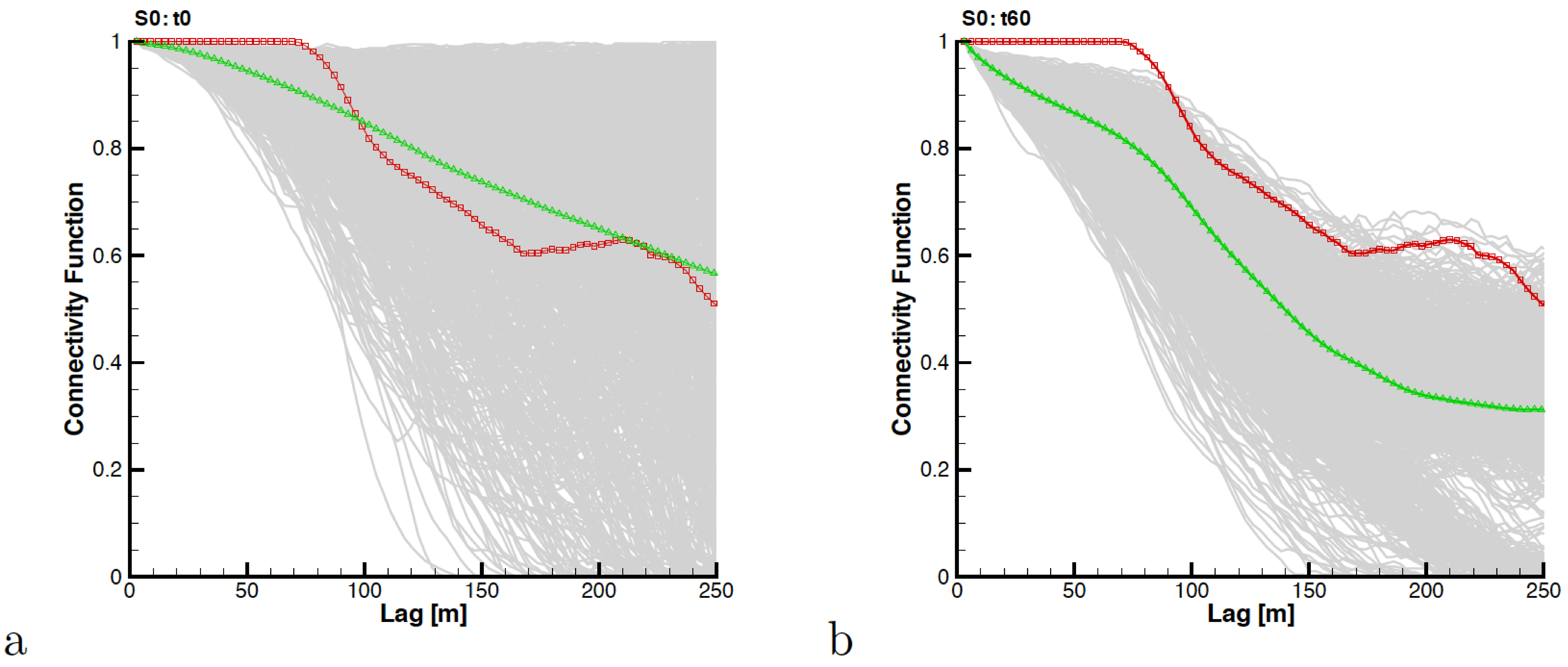

Figure 24: Scenarios S0. Connectivity curves for the initial ensemble of realizations and for the updated realizations after the 60th assimilation time step. The red square line corresponds to the connectivity curve in the reference, the green delta line corresponds to the mean of the ensemble, and the gray lines correspond to the individual realizations.

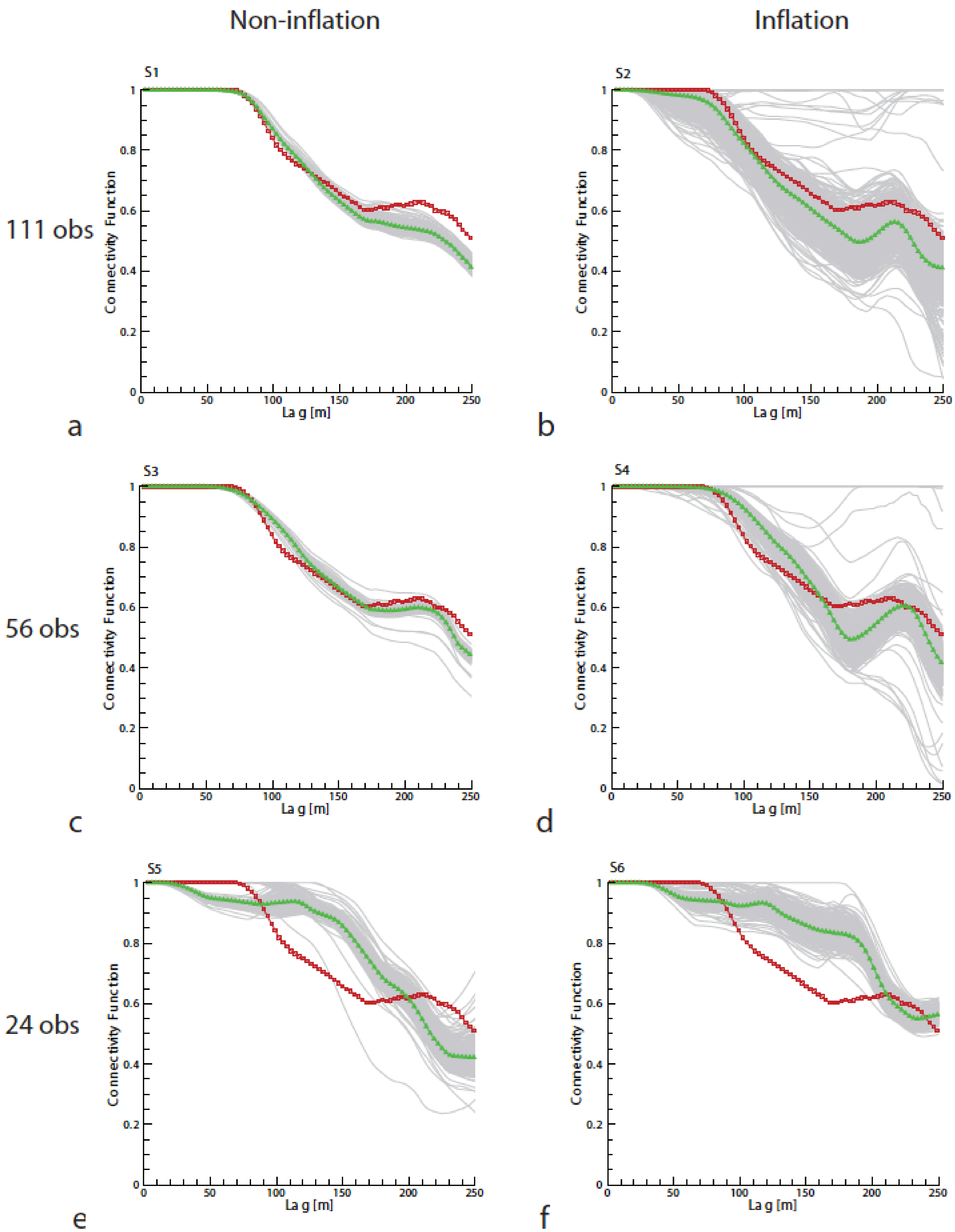

Figure 25: Scenarios S1-S6. Connectivity curves. The red square line corresponds to connectivity curves in the reference, the green delta line corresponds to the mean of the ensemble, and the gray lines correspond to the individual realizations